

# Nonlinear Coupling of Kinetic Alfvén Waves and Ion Acoustic Waves in the Inner Heliosphere

Mani K Chettri <sup>1</sup>, Vivek Shrivastav <sup>1</sup>, Rupak Mukherjee <sup>1</sup>, Nidhi Gaur <sup>2</sup>, R. P. Sharma <sup>3</sup>, and Hemam D. Singh <sup>1</sup> Department of Physics, Sikkim University, Gangtok, Sikkim, India; hdsingh@cus.ac.in <sup>2</sup> DAV Public School, Sector 14, Gurugram, Haryana, India <sup>3</sup> Plasma Simulation Laboratory, Department of Energy Science and Engineering, Indian Institute of Technology Delhi, Delhi, India Received 2024 June 13; revised 2024 August 28; accepted 2024 August 31; published 2024 October 2

#### **Abstract**

We study the nonlinear coupling of kinetic Alfvén waves with ion acoustic waves applicable to the Earth's radiation belt and near-Sun streamer belt solar wind using dynamical equations in the form of modified Zakharov systems. Numerical simulations show the formation of magnetic field filamentary structures associated with density humps and dips which become turbulent at later times, redistributing the energy to higher wavenumbers. The magnetic power spectra exhibit an inertial range Kolmogorov-like spectral index value of -5/3 for  $k_\perp \rho_i < 1$ , followed by a steeper dissipation range spectra with indices  $\sim -3$  for the radiation belt case and  $\sim -4$  for the near-Sun streamer belt solar wind case, here  $k_\perp$  and  $\rho_i$  represent the wavevector component perpendicular to the background magnetic field and the ion thermal gyroradius, respectively. Applying quasilinear theory in terms of the Fokker–Planck equation in the region of wavenumber turbulent spectra, we find the particle distribution function flattening in the superthermal tail population which is the signature of particle energization and plasma heating.

Key words: Sun: chromosphere – Sun: corona – Sun: heliosphere

## 1. Introduction

One of the outstanding problems in solar physics is the heating of the solar corona up to millions of Kelvin (K), much greater than the Sun's inner surfaces, photosphere (≈5700 K) and chromosphere ( $\approx$ 50,000 K) allowing the direction of energy flow opposite to the temperature gradient unlike the usual modes of energy transportation via convection, conduction and radiation. Also, in the Earth's magnetosphere, the transfer of energy stored in the magnetotail into the low altitudes of the Earth's atmosphere remains unresolved. The magnetic reconnection and wave-heating models (Fisk 2003; McComas et al. 2007; Velli et al. 2015) are broadly accepted mechanisms for energy conversion in space and the magnetospheric plasmas. Many theoretical studies have shown that in a magnetized plasma environment, Alfvén waves can heat the plasma via wave dissipation (Del Zanna & Velli 2002; Escande et al. 2019) and accelerate the solar wind through the action of wave pressure (Alazraki & Couturier 1971; Suzuki & Inutsuka 1971). These theories are supported by many spacecraft observations showing various signatures of Alfvénic perturbations in the photosphere (Song & Vasyliūnas 2011) and chromosphere of the Sun (Grant et al. 2018), solar coronal regions (Sharma Pyakurel et al. 2018; Kasper et al. 2021) and solar wind flowing at various regions of the heliosphere (Chaston et al. 2000, 2005a; Raghav & Kule 2018; D'Amicis et al. 2021a, 2021b; Kasper et al. 2021). These observations not

only corroborate the existence of Alfvén waves but also quantify their energy contributions to the coronal heating problem and solar wind acceleration (McComas et al. 2007; Liu et al. 2014; Chae et al. 2021), bridging theoretical predictions with empirical evidence.

The magnetohydrodynamic (MHD) Alfvén waves become dispersive when the transverse spatial length scale (wavelength) is comparable to the electron inertial scale (Goertz & Boswell 1979) or the ion gyroradius (Stéfant 1970; Hasegawa 1976). Dispersive Alfvén waves can be classified into two categories, kinetic and inertial depending on specific local plasma properties (Shukla et al. 2009; Rai et al. 2017; Barik et al. 2021). If the electron thermal speed is greater than the local Alfvén speed  $(v_A)$ , the wave is kinetic which is valid in hot plasma having  $\beta_e \gg m_e/m_i$ , where  $\beta_e (=8\pi n_e T_e/B_0^2)$  is the ratio of the electron thermal pressure to the magnetic pressure,  $m_e$   $(m_i)$  is the mass of an electron (ion),  $n_e$  is the electron density,  $T_e$  is the electron temperature, and  $B_0$  is the background (ambient) plasma magnetic field. If the electron thermal speed is less than  $v_A$ , the wave is inertial which is valid for cold plasma having  $\beta_e \ll m_e/m_i$ . These two kinds of dispersive Alfvén waves are commonly known as kinetic Alfvén waves (KAWs) which can be differentiated by high  $\beta$ and low  $\beta$ . They retain some blasic properties of MHD Alfvén waves such as currents along the magnetic field lines and quasiparallel group velocity. However, the ions no longer follow the

ambient magnetic field lines but the electrons follow it due to the smaller gyroradius when the wave dynamics are faster than the ion orbital motions (Hasegawa 1976; Johnson & Cheng 1997; Hollweg 1999). These unmatched motions between electrons and ions develop charge separation generating a parallel electric field that can heat plasma particles along the ambient magnetic field lines (Tsiklauri 2006; Cheng et al. 2016).

The existence of KAWs can be identified by measuring the ratio of electric and magnetic field fluctuations perpendicular to the background magnetic field  $(\delta E_{\perp}/\delta B_{\perp})$ , calculated from the spectra of satellite observations and comparing it with the theoretical predictions (Chen et al. 2021b). For long wavelength shear Alfvén waves, this ratio is  $v_A$ . By analyzing the Parker Solar Probe (PSP) spacecraft data during its first near-Sun encounter, Malaspina et al. (2022) showed that the ratio is greater than  $v_A$  for low-frequency  $\approx 1$  Hz, matching the theoretical prediction calculated by Stasiewicz et al. (2000) by combining the dispersion relation and polarization properties of KAWs in the low-frequency limit ( $\omega \ll \omega_{ci}$ ) as

$$\frac{|\delta E_{\perp}|}{|\delta B_{\perp}|} = \frac{v_A (1 + k_{\perp}^2 \rho_i^2)}{\sqrt{1 + k_{\perp}^2 (\rho_s^2 + \rho_i^2)}},\tag{1}$$

where  $\omega$  is the frequency of the pump KAW,  $\omega_{ci}$  is the ion gyro-frequency,  $\rho_i = v_{ti}/\omega_{ci}$  is the ion thermal gyroradius,  $v_{ti}$  (= $\sqrt{\gamma_i k_{\rm B} T_i/m_i}$ ) is the thermal speed of ion,  $\rho_s = v_{te}/\omega_{ci}$  is the ion gyroradius at electron temperature,  $v_{te}$  (= $\sqrt{\gamma_e k_{\rm B} T_e/m_e}$ ) is the thermal speed of electrons,  $\gamma_e(\gamma_i)$  is the ratio of specific heats  $(c_p/c_v)$  for electrons (ions), and  $k_{\perp}$  represents the wavevector component perpendicular to the background magnetic field direction. At frequencies  $\omega > \omega_{ci}$ , the discrepancies between the theoretical and observational values of  $\delta E_{\perp}/\delta B_{\perp}$  arise which may be due to the observations reaching the noise level of the instruments and as well as non-inclusion of the additional terms like  $(1-\omega^2/\omega_{ci}^2)$  in the theory (Salem et al. 2012).

Numerous observational studies from Polar, Cluster, Viking, Freja and Fast Auroral SnapshoT (FAST) spacecraft have provided compelling evidence for the prevalence of KAWs in various regions of the Earth's magnetosphere (Johnson et al. 2001; Chaston et al. 2005b; Dai 2009; Duan et al. 2012, 2016). Van Allen Probe measurements have revealed the existence of KAWs in the inner magnetosphere (Chaston et al. 2015, 2018), predominantly because of the injections from the magnetotail (Ripoll et al. 2020). Near the Earth's plasma sheet regions, KAWs are excited at the onset of substorm events, resulting from gradients in particle number density and magnetic field strength (Duan et al. 2012). The fluctuating fields of KAWs can have frequencies of  $\approx$ 0.2–20 Hz in the spacecraft frame in the Earth's plasma sheet located at 6–30 Earth-radii ( $R_{\rm E}$ ) (Chaston et al. 2012). At the plasma sheet boundary layer around  $6R_{\rm E}$ , the KAWs have frequencies of 1-4 Hz, while the shear Alfvén

waves (for which kinetic effects are negligible) can have frequencies ≈15-50 mHz (Keiling et al. 2005; Zhang et al. 2022). Earlier observations of KAWs mostly occurred in the solar wind at 1 au within a frequency range slightly beyond or less than ten times the ion gyro-frequency. Most recently, the PSP has reached 0.0485 au distance from the Sun's center as of 2023 September 27 (Johns Hopkins University Applied Physics Laboratory 2023), providing us with a test of whether solar wind electromagnetic fluctuations exhibit KAW properties at frequencies extending well beyond the ion gyrofrequency range. To investigate the presence of higher frequency whistler modes, the ratio of the magnetic field fluctuations along the ambient magnetic field  $(\delta B_{\parallel})$  to the fluctuations of the total magnetic field ( $\delta B$ ) were evaluated from the observational spectra, as a function of frequency (Chaston et al. 2009; Shaikh & Zank 2009). It confirmed the dominance of KAWs at 1 au over whistler modes below the gyroscale (Bale et al. 2005; Sahraoui et al. 2010). In the near-Sun solar wind, Malaspina et al. (2022) calculated this ratio by analyzing the PSP spacecraft data and found that at lowfrequency, the ratio is small, then increases until the frequency where the Alfvén waves become dispersive, then remains constant below 1. All these characteristics support the presence of KAW fluctuations in the near-Sun solar wind. In fact, the KAW mode is considered as one of the likely fluctuation constituents in solar wind turbulence. The fluctuations in electromagnetic fields and particle velocities are evident from the in situ observations in the solar wind (Tu & Marsch 1995; Alexandrova et al. 2013; Bruno & Carbone 2013) and planetary magnetosheaths (Chen & Boldyrev 2017; Matteini et al. 2017; Roberts et al. 2019). The fluid like turbulent cascades with eddies and fluctuations lead to the transfer of energy from large scales (deposited into the system before undergoing turbulence) to smaller scales. At the scales smaller than the particle gyration scales, the particles decouple from the magnetic field, leading to efficient transfer of field energy to particles' bulk kinetic and internal energies (Roberts et al. 2022). This evidence can be used as a model to study how the KAW turbulence fits into the macroscopic scales such as solar wind, particle acceleration and energization of the plasma through dissipation. The physics behind the particle acceleration and plasma heating in heliospheric plasma is unresolved. Some proposed mechanisms are the damping of electromagnetic waves (Cuseri et al. 1999) and dissipation in coherent structures (Zhdankin et al. 2014). Several theoretical models, such as phase mixing (Heyvaerts & Priest 1983), turbulent cascade (Matthaeus et al. 1999), resonant absorption (Goossens et al. 2011) and magneto-acoustic oscillations (Hashim et al. 2021), have been proposed to understand the dissipation mechanism in the solar wind, although there is no generally agreed mechanism due to variations in dissipation rates, length scales and the physics involved.

Previous studies, including observations by PSP and Solar Orbiter, have unveiled a broad power spectrum in turbulent solar wind fluctuations, spanning timescales from several hours down to approximately 0.01 s in spacecraft reference frames (Alexandrova et al. 2013; Telloni et al. 2021; Šafránková et al. 2023). Using MHD turbulence theory reveals that magnetic field spectra in the inertial range is predominantly oriented perpendicular to the mean magnetic field direction (Bale et al. 2005; Chen et al. 2011). Specifically, the spectral index at 1 au approaches  $\approx -5/3$  in the inertial range, gradually steepening to spectral indices between -2 and -4 at smaller kinetic scales (Alexandrova et al. 2009; Chen et al. 2013; Chen & Zonca 2016). Similar trends of -5/3 in the inertial range and much steeper at the kinetic scale were also reported from PSP observations (Chen et al. 2020; Shi et al. 2021; Lotz et al. 2023; Šafránková et al. 2023). In the dissipation range, Šafránková et al. (2023) found a spectral index of -4.8 at the closest approach (0.12 au) to the Sun then becoming flatter as it moves away, approaching  $\approx -3$  at around 0.4 au. From 0.4 to 1 au, the spectral indices remain approximately constant (-5/3) at inertial and  $\approx -3$  at dissipation range).

Our present work focuses on the nonlinear interactions of KAWs and ion acoustic waves applicable for an arbitrary  $\beta$ plasma (both  $\beta < 1$  and  $\beta > 1$ ) by taking the non-adiabatic response of the background density in the presence of a nonlinear ponderomotive force. The PSP provides us with adequate data to analyze the plasma properties in sub-Alfvénic and super-Alfvénic flows covering many solar regions of low, intermediate and high  $\beta$  plasmas (Larosa 2021; Zhao et al. 2022b). The inner corona features closed magnetic fields and plasma  $\beta < 1$ , transitioning to open fields and higher  $\beta$  values in the middle region. In this paper, we have derived the model equations in the form of generalized Zakharov equations, called the modified Zakharov System of Equations (modified ZSEs). The equations were solved numerically to understand the solar wind turbulence near the Earth and the Sun. The numerical simulation results showed coherent magnetic filamentary structures of KAWs associated with density humps and dips becoming turbulent as time evolves, indicating the redistribution of energy among the higher wavenumbers. Many authors (Shukla et al. 2004; Singh & Sharma 2006; Kumar et al. 2009; Yadav & Sharma 2014; Singh & Jatav 2019a) have studied the wave turbulence generated because of the interaction of KAWs and ion acoustic waves by taking the adiabatic and nonadiabatic response of the background density. However, all these studies were limited only to low  $\beta$  < 1. Recently, Singh et al. (2022) and Dewan et al. (2022) studied the magnetic turbulence applicable for arbitrary  $\beta$  plasma when the pump KAWs interact with low-frequency magnetosonic waves (Singh et al. 2022) and high-frequency oblique whistler waves (Dewan et al. 2022) to understand the role of plasma  $\beta$  in the laboratory and astrophysical plasmas. Although they have used the model applicable to all the ranges of plasma  $\beta$ , they have

considered high  $\beta \sim 100$  for the sake of illustration only without applying it to any real laboratory or space plasma environments. Moreover, these studies were limited to the situations where KAW frequency is much less than the ion cyclotron frequency. In this paper, we have considered the coupling of pump KAWs and ion acoustic waves (and rederived the model equations when KAW frequency is not necessarily less than ion cyclotron frequency) for  $\beta \approx 0.0041$ and  $\beta \approx 6.940$  applicable for near-Earth radiation belt and near-Sun streamer belt solar wind, respectively. To study space plasma turbulence, various low-frequency waves have been considered in the past like magnetosonic, ion acoustic or other low-frequency waves. Here, to illustrate our viewpoint in this article, we have taken a low-frequency wave to be an ion acoustic wave but it will be certainly interesting to consider the effect of different low-frequency waves (for example magnetosonic waves) on the evolution of turbulence. We are planning to do this in the future. The framework of the present paper is organized as follows: the model equations in the form of modified ZSEs are derived in Section 2, the numerical simulation results are presented in Section 3, the particle heating as evident from the superthermal tail expansion of the distribution function is examined in Section 4, and finally, Section 5 summarizes the overall results of the present investigation.

## 2. Model Equations

## 2.1. Dynamics of Pump KAW

We consider a collisionless, non-relativistic two-fluid (electrons and protons as ions) magnetoplasma having a uniform background magnetic field  $\mathbf{B_0} = (0, 0, B_0)$  and the electric field  $\mathbf{E} = \delta \mathbf{E}$ , where  $\delta \mathbf{E}$  is the fluctuating component. In our geometry, the z-direction is parallel to  $\mathbf{B_0}$  and the pump KAW propagates in the x-z plane such that the wavevector  $\mathbf{k_0} = k_{0x}\hat{x} + k_{0z}\hat{z}$ , where all the wave variations are in the x-z plane, i.e.,  $(\partial/\partial x, 0, \partial/\partial z)$ , except the induced magnetic field perturbations in the y-direction  $(\delta B_y)$ . The directions along and across  $\mathbf{B_0}$  are denoted as parallel and perpendicular directions, respectively. The linearized continuity and momentum equations are

$$\frac{\partial \delta n_s}{\partial t} + n_{0s} \nabla \cdot \delta \mathbf{v}_s \approx 0, \tag{2}$$

and

$$m_s \frac{\partial \delta \mathbf{v}_s}{\partial t} \approx q_s \delta \mathbf{E} + \frac{q_s}{c} (\delta \mathbf{v}_s \times \mathbf{B}_0) - \frac{\gamma_s k_B T_s}{n_{0s}} \nabla \delta n_s,$$
 (3)

respectively, where s indicates the species of the particles: electrons (e) and ions (i),  $m_s$ ,  $q_s$ ,  $T_s$ ,  $n_{0s}$  represent the mass, charge, temperature and average density of the species s respectively; c is the speed of light,  $\delta n_s$  is the fluctuation in number density,  $\delta v_s$  is the bulk velocity ( $v = \delta v_s$ , with no mean

flow velocity),  $\gamma_s$  is the ratio of specific heats  $(c_p/c_v)$  and  $k_B$  is the Boltzmann constant. Additionally, we assume a quasineutrality condition:  $n_{0e} \simeq n_{0i} \simeq n_0$  and  $\delta n_e \simeq \delta n_i \simeq \delta n$  in both equilibrium and the perturbed state, the isothermal condition:  $\gamma_e = \gamma_i = 1$  and small perturbations:  $\delta n_s/n_{0s} \ll 1$  and  $\delta B_y/B_0 \ll 1$ . It may be mentioned here that in deriving the linearized equations we have neglected the nonlinear term  $(v.\nabla)v$  in the convective derivative  $(\partial/\partial t + v.\nabla)$ , valid for weak dispersion to avoid the vector nonlinearity (Sadiq et al. 2018). Even if it is not for weak dispersion, the convective term can be neglected for the perpendicular motion (Kaur & Saini 2016; Sadiq et al. 2018; Singh et al. 2021).

From Equation (3), assuming all the first-order fluctuations to be of the form  $\delta f = \delta f e^{i(k_{0x}x+k_{0z}z-\omega t)}$ , where  $\omega$  is the frequency of the pump KAW, we can separate the electron and ion velocity components, respectively, as

$$\delta v_{ex} = \frac{1}{\omega_{ce}^2 - \omega^2} \frac{e}{m_e} \left( i\omega \delta E_x + \omega_{ce} \delta E_y + i\omega \frac{\gamma_e k_B T_e}{n_0 e} \frac{\partial \delta n}{\partial x} \right), \tag{4}$$

$$\delta v_{ey} = \frac{e\delta E_y}{\omega_{ce}^2 - \omega^2} \frac{i\omega}{m_e} - \frac{e}{m_e} \frac{\omega_{ce}}{\omega_{ce}^2 - \omega^2} \left( \delta E_x + \frac{\gamma_e k_B T_e}{n_0 e} \frac{\partial \delta n}{\partial x} \right), \tag{5}$$

$$\delta v_{ez} = \frac{e\delta E_z}{m_e} \frac{1}{i\omega} + \frac{1}{i\omega} \frac{\gamma_e k_B T_e}{n_0 m_e} \frac{\partial \delta n}{\partial z}, \tag{6}$$

$$\delta v_{ix} = \frac{e}{m_i} \frac{1}{\omega_{ci}^2 - \omega^2} \left( \omega_{ci} \delta E_y - i\omega \left( \delta E_x - \frac{\gamma_i k_B T_i}{n_0 e} \frac{\partial \delta n}{\partial x} \right) \right), \quad (7)$$

$$\delta v_{iy} = -\frac{e}{m_i} \frac{\omega_{ci}}{\omega_{ci}^2 - \omega^2} \left( i \frac{\omega \delta E_y}{\omega_{ci}} + \delta E_x - \frac{\gamma_i k_B T_i}{n_0 e} \frac{\partial \delta n}{\partial x} \right), \quad (8)$$

and

$$\delta v_{iz} = -\frac{e\delta E_z}{m_i} \frac{1}{i\omega} + \frac{1}{i\omega} \frac{\gamma_i k_B T_i}{n_0 m_i} \frac{\partial \delta n}{\partial z}, \tag{9}$$

where  $\omega_{ce} = eB_0/m_e c$  is the electron cyclotron frequency and  $\omega_{ci} = eB_0/m_i c$  is the ion cyclotron frequency.

The electron and ion continuity equations can be respectively written as

$$\frac{\partial \delta n_e}{\partial t} + n_0 \left( \frac{\partial \delta v_{ex}}{\partial x} + \frac{\partial \delta v_{ez}}{\partial z} \right) = 0, \tag{10}$$

and

$$\frac{\partial \delta n_i}{\partial t} + n_0 \frac{\partial \delta v_{ix}}{\partial x} = 0. \tag{11}$$

In writing Equation (11), we neglected the parallel ion motion because of the larger mass and Larmor radius; its motion spends much of the time in the perpendicular direction.

From Equation (10), neglecting the perpendicular electron motion due to its small polarization drift velocity because of

small mass and Larmor radius, we get

$$\delta n_e = \frac{n_0 k_{0z}}{\omega} \delta v_{ez},\tag{12}$$

and substituting it into Equation (6) we get

$$\delta v_{ez} = \frac{e\delta E_z}{i\omega m_e} + \left(\frac{\gamma_e k_{\rm B} T_e}{m_e}\right) \frac{k_{0z}^2}{\omega^2} \delta v_{ez}.$$
 (13)

Using the dispersion relation of shear Alfvén wave  $v_A = \omega/k_{0z}$ , the ion acoustic speed  $c_s = \sqrt{k_{\rm B}(\gamma_e T_e + \gamma_i T_i)/m_i}$  with the isothermal conditions,  $\gamma_e = \gamma_i$  and  $T_e = T_i = T$ , and denoting plasma  $\beta$  as  $8\pi n_0 k_{\rm B} T/B_0^2 = c_s^2/v_{\rm A}^2$ ), the above Equation (13) becomes

$$\frac{m_e}{m_i}\delta v_{ez} = \frac{e\delta E_z}{i\omega m_i} + \frac{\beta}{2}\delta v_{ez}.$$
 (14)

In Equation (14), if we consider only plasma for which  $\beta \gg (m_e/m_i)$ , the left-hand side representing the electron inertial term can be neglected. Since our study is based on any arbitrary  $\beta$  we will retain this term.

Using Faraday's law

$$\nabla \times \boldsymbol{E} = -\frac{1}{c} \frac{\partial \boldsymbol{B}}{\partial t},\tag{15}$$

and taking the y-component and differentiating with respect to (w.r.t.) "t," we get

$$\frac{\partial^2(\delta B_y)}{\partial t^2} = c \frac{\partial^2(\delta E_z)}{\partial t \partial x} - c \frac{\partial^2(\delta E_x)}{\partial t \partial z}.$$
 (16)

To obtain the dynamical equation satisfied by the transverse perturbed magnetic fields of the pump KAWs, first, we will express the perpendicular and parallel perturbed electric fields  $\delta E_x$  and  $\delta E_z$  respectively in terms of  $\delta B_y$ . Subtracting electron and ion continuity equations, and using the quasineautrality condition, we get the conservation law of current density as

$$\nabla \cdot \boldsymbol{J} = 0, \tag{17}$$

where the current density  $J = e n_0 (\delta v_i - \delta v_e)$ .

In KAWs, as the perpendicular wavelength is comparable to the ion gyroradius, the ion transverse motion is modified by the finite ion gyroradius effects. This is because of the non-uniformity of the wave electric field, the ions encounter significantly different electric fields during the different phases of the gyromotion. So, ions cannot follow the  $E \times B$  drift in the electric field of KAWs while electrons are still frozen-in to the wave field. The difference in transverse motion of ions and electrons introduces a charge separation and coupling to the electrostatic mode (Hasegawa & Uberoi 1978). Accordingly, a quasi-electrostatic electric field is developed in the transverse direction. To preserve the quasi-neutral condition, electrons quickly move along the magnetic field. Therefore, we can neglect the transverse motion (polarization drift) of the electrons as compared to the ions. Moreover, the ion motion

along the magnetic field lines is neglected here, because we want to separate only the KAW mode, otherwise it will couple with other kinds of wave modes such as fast, slow and Alfvén modes as illustrated by Hollweg (1999). The parallel motion of electrons generates the field aligned current  $(\delta J_z)$  of KAWs that induces a wave magnetic field  $\delta B_y$  perpendicular to the DC magnetic field in accordance with Ampere's law  $i\mathbf{k} \times \delta \mathbf{B} = \delta \mathbf{J}$ . Therefore, the existence of KAWs can be confirmed by measuring the ratio of the wave electric field to the wave magnetic field  $|\delta E_x/\delta B_y|$  as given in Equation (1).

The velocity components form, Equation (17) can be written as

$$en_0 \left( \frac{\partial (\delta v_{ix})}{\partial x} - \frac{\partial (\delta v_{ez})}{\partial z} \right) = 0.$$
 (18)

Substituting the expressions for  $\delta v_{ez}$  and  $\delta v_{ix}$  given by Equations (6) and (7), and using  $\frac{\partial}{\partial t} \rightarrow (-i\omega)$ , the above equation is transformed to

$$\frac{\partial^2 (\delta E_x)}{\partial t \partial x} = -\frac{\partial (\delta E_y)}{\partial x} \omega_{ci} + (\omega_{ci}^2 - \omega^2) \frac{m_i}{e} \frac{\partial (\delta v_{ez})}{\partial z}.$$
 (19)

We can write Ampere's law as

$$\nabla \times \mathbf{B} = \frac{4\pi}{c} \mathbf{J},\tag{20}$$

here we have neglected the displacement current because of the low-frequency assumption,  $\omega \ll \omega_{pe}$ , where  $\omega_{pe}$  is the electron plasma frequency expressed as  $\sqrt{4\pi n_0 e^2/m_e}$ . In such a situation, the phase velocity of the wave is much smaller than the speed of light. If we assume the characteristic time and length scales are  $\tau$  and l respectively, then  $\partial/\partial t \sim \tau^{-1}$ ,  $\nabla \sim l^{-1}$  and phase velocity  $v_{\rm ph} \sim l/\tau$ . Again, Faraday's law gives the scaling  $\frac{E}{B} \sim \frac{v_{\rm ph}}{c}$ . Now, comparing the magnitudes of the displacement current and the left-hand side of Equation (20), we get  $\frac{\partial E/\partial t}{c\nabla \times B} \sim \frac{E/\tau}{cB/l} \sim \frac{v_{\rm ph}^2}{c^2} \ll 1$  as  $v_{\rm ph} \ll c$ .

Taking the z-component of Equation (20) and differentiating it w.r.t. "t", we get

$$\frac{\partial^2 (\delta B_y)}{\partial t \partial x} = \frac{4\pi}{c} \frac{\partial J_z}{\partial t}.$$
 (21)

Here, the parallel component of the current density is entirely carried by the electron's motion, i.e.,  $J_z = -en_e\delta v_{ez}$ . Substituting the expression for  $J_z$  along with  $n_e = n_0 + \delta n$ , we get

$$\frac{\partial^{2}(\delta B_{y})}{\partial t \partial x} = \frac{\omega_{pe}^{2}}{c} \left( 1 + \frac{\delta n}{n_{0}} \right) \left( \delta E_{z} + \frac{\gamma_{e} k_{B} T_{e}}{e n_{0}} \frac{\partial (\delta n)}{\partial z} \right). \tag{22}$$

The parallel component of the electric field can be written from Equation (22) as

$$\delta E_z = \frac{c}{\omega_{pe}^2} \frac{\partial^2 (\delta B_y)}{\partial t \partial x} \left( 1 - \frac{\delta n}{n_0} \right) - \frac{\gamma_e k_B T_e}{e n_0} \frac{\partial (\delta n)}{\partial z}.$$
 (23)

This expression for  $\delta E_z$  can be used to find out  $\delta v_{ez}/\partial z$  from Equation (6) to get

$$\frac{\partial(\delta v_{ez})}{\partial z} = \frac{ec}{i\omega} \frac{1}{\omega_{ne}^2 m_e} \frac{\partial^3 (\delta B_y)}{\partial t \partial x \partial z} \left( 1 - \frac{\delta n}{n_0} \right). \tag{24}$$

Putting Equation (24) into Equation (19), we get

$$\frac{\partial(\delta E_x)}{\partial t} = -\omega_{ci}\delta E_y - \frac{m_i c(\omega_{ci}^2 - \omega^2)}{m_e \omega_{pe}^2} \frac{\partial(\delta B_y)}{\partial z} \left(1 - \frac{\delta n}{n_0}\right). \tag{25}$$

The z-component of Faraday's law (15) is given as

$$\delta E_{y} = (\omega/ck_{0x})\delta B_{z}. \tag{26}$$

In the case of low-frequency  $\omega \ll \omega_{ci}$  and low plasma  $\beta$  approximation, the compressive component of the magnetic field perturbation  $(\delta B_z)$  will play no significant contribution, i.e., we can take  $\delta B_z = 0$  (Howes et al. 2006; Schekochihin et al. 2009; Cramer 2011). However, for arbitrarily finite  $\beta$  consideration, the parallel component of the magnetic field perturbation should be taken into account and can be calculated from the pressure balance equation  $\nabla (k_B T \delta n_e + \delta B_z^2/8\pi) = 0$ . This gives  $\delta B_z/B_0 = -\beta \delta n_e/2n_0$  (as obtained by Hollweg (1999) in Equation (14)) which indicates a strong anticorrelation between the magnetic and thermal pressures. It is used to examine the density and magnetic field fluctuations observed in the inertial range of the magnetic field turbulence spectra (Burlaga et al. 1990; Roberts 1990). Furthermore, by using the continuity Equation (2) and Ampere's law (20) we get

$$\delta B_z = -\frac{\beta}{2} \frac{\omega_{ce} c^2}{\omega_{ne}^2} \frac{k_{0x}}{\omega} \frac{\partial (\delta B_y)}{\partial z}.$$
 (27)

Then, Equation (27) can be deduced as

$$\frac{\delta B_z}{\delta B_y} = -\frac{ik_{0x}k_{0z}c_s^2}{\omega\omega_{ci}},\tag{28}$$

which is consistent with Equation (11) obtained by Hollweg (1999).

Substituting Equations (26) and (27) into Equation (25) and differentiating once w.r.t. "z" we get

$$\frac{\partial^{2}(\delta E_{x})}{\partial t \partial z} = \frac{\omega_{ci} \beta B_{0}}{8\pi e n_{0}} \frac{\partial^{2}(\delta B_{y})}{\partial z^{2}} - \frac{v_{A}^{2}}{c\omega_{ci}^{2}} (\omega_{ci}^{2} - \omega^{2}) \frac{\partial^{2}(\delta B_{y})}{\partial z^{2}} \left(1 - \frac{\delta n_{s}}{n_{0}}\right). \tag{29}$$

Differentiating  $J_z$  w.r.t. "t" we get

$$\frac{\partial J_z}{\partial t} = n_e e \left( \frac{e \delta E_z}{m_e} + \frac{\gamma_e k_B T_e}{n_e m_e} \frac{\partial \delta n_e}{\partial z} \right). \tag{30}$$

By calculating  $J_z$  from Ampere's law (20) and substituting it into Equation (30) we get

$$\frac{\partial(\delta E_z)}{\partial t} = \frac{\lambda_e^2}{c} \frac{\partial^3(\delta B_y)}{\partial t^2 \partial x} - \frac{v_{te}^2 \lambda_e^2}{c} \frac{\partial^3(\delta B_y)}{\partial x \partial z^2},\tag{31}$$

where  $\lambda_e = c/\omega_{pe}$  is the electron inertial length.

Differentiating Equation (31) w.r.t. "x" and substituting it to Equation (16) along with Equation (29), we get the following dynamical equation

$$\frac{\partial^{2}(\delta B_{y})}{\partial t^{2}} - \lambda_{e}^{2} \frac{\partial^{4}(\delta B_{y})}{\partial t^{2} \partial x^{2}} + v_{te}^{2} \lambda_{e}^{2} \frac{\partial^{4}(\delta B_{y})}{\partial x^{2} \partial z^{2}} + \frac{B_{0} c \beta \omega_{ci}}{8\pi n_{0} e} \frac{\partial^{2}(\delta B_{y})}{\partial z^{2}} - v_{A}^{2} \left(\frac{\omega_{ci}^{2} - \omega^{2}}{\omega_{ci}^{2}}\right) \left(1 - \frac{\delta n}{n_{0}}\right) \frac{\partial^{2}(\delta B_{y})}{\partial z^{2}} = 0.$$
(32)

By performing the Fourier transform in the linear part of Equation (32), we get the linear dispersion relation of KAWs as

$$\frac{\omega^2}{k_{0z}^2} = v_A^2 \left( \frac{1 + \rho_i^2 k_{0x}^2 + (\beta/2)}{1 + \lambda_e^2 k_{0x}^2 + \lambda_i^2 k_{0z}^2} \right).$$
(33)

Equation (33) resembles, but does not agree with, the dispersion relation of KAWs as shown in Equation (42) published by Hollweg (1999). This is mainly because, in the derivation of Hollweg (1999), the parallel ion velocity  $\delta v_{iz}$  was considered. Because of this, fast, slow and Alfvén modes were coupled together in the dispersion relation Equation (41) of Hollweg (1999) and the dispersion relation corresponding to KAW was separated later (Equation (42) of Hollweg 1999) by considering several assumptions. In our case, we have already neglected  $\delta v_{iz}$ , the reason being described earlier, so no mode coupling occurs. However, we can expand Equation (41) of Hollweg (1999) at ion gyroscale with  $k_\perp \rho_i \ll 1$ ,  $k_\perp \lambda_e \ll 1$  and  $k_\perp \lambda_e \ll k_\perp \rho_i$  to obtain, to second order,

$$\frac{\omega^2}{k_{\parallel}^2 v_A^2} = 1 + k_{\perp}^2 \rho_i^2 - k_{\perp}^4 \rho_i^4 \beta. \tag{34}$$

The term  $\lambda_i^2 k_{0z}^2$  in the denominator of Equation (33) is due to the finite frequency effect. For  $\omega \ll \omega_{ci}$  (i.e.,  $\lambda_i k_{0z} \ll 1$ ) and  $\lambda_e k_{0x} \ll 1$ , our dispersion relation Equation (33) can be compared with that of Hollweg (1999) as deduced above (Equation (34)), except in the coefficient of  $\beta$ . Further, if we neglect the effect of the finite beta correction, our dispersion relation Equation (33) can be transformed for  $m_e/m_i \ll \beta \ll 1$  as  $\omega^2 = v_A^2 k_{0z}^2 (1 + k_{0x}^2 \rho_i^2)$  (Shukla & Stenflo 2005) in the limit of  $\lambda_e k_{0x} \ll 1$  and  $\lambda_i k_{0z} \ll 1$ .

The dynamical Equation (32) is satisfied by the magnetic field perturbations of pump KAWs. One of the possible solutions of Equation (32) is a plane wave (linearly polarized) having base frequency  $\omega$ , modulated by a slowly varying envelope  $\delta \tilde{B}_{y}$  which is expressed as

$$\delta B_{\rm v} = \delta \tilde{B}_{\rm v}(x, z, t) e^{i(k_{0x}x + k_{0z}z - \omega t)}, \tag{35}$$

where  $\delta \tilde{B}_y(x, z, t)$  is the inhomogeneous amplitude of the transverse pump KAW magnetic field slowly varying in space in comparison to the exponential part  $e^{i(k_{0x}x+k_{0z}z-\omega t)}$ .

Substituting Equation (35) into (32), we get the envelope equation of the KAWs as

$$2i\omega(1 + \lambda_{e}^{2}k_{0x}^{2})\frac{\partial(\delta\tilde{B}_{y})}{\partial t} + 2i(k_{0x}\lambda_{e}^{2}k_{0z}^{2}v_{te}^{2} - k_{0x}\lambda_{e}^{2}\omega^{2})\frac{\partial(\delta\tilde{B}_{y})}{\partial x}$$

$$+ (v_{te}^{2}\lambda_{e}^{2}k_{0z}^{2} - \lambda_{e}^{2}\omega^{2})\frac{\partial^{2}(\delta\tilde{B}_{y})}{\partial x^{2}}$$

$$+ \left[k_{0z}v_{te}^{2}\lambda_{e}^{2} + \frac{cB_{0}\beta\omega_{ci}}{8\pi n_{0}e} + v_{A}^{2}\left(1 - \frac{\omega^{2}}{\omega_{ci}^{2}}\right)\right]\frac{\partial^{2}(\delta\tilde{B}_{y})}{\partial z^{2}}$$

$$+ 2ik_{0z}\left[v_{te}^{2}\lambda_{e}^{2}k_{0x}^{2} + v_{A}^{2}\left(1 - \frac{\omega^{2}}{\omega_{ci}^{2}}\right) + \frac{cB_{0}\beta\omega_{ci}}{8\pi n_{0}e}\right]$$

$$\times \frac{\partial(\delta\tilde{B}_{y})}{\partial z} + 4\lambda_{e}^{2}k_{0x}\omega\frac{\partial^{2}(\delta\tilde{B}_{y})}{\partial t\partial x}$$

$$- 2i\omega\lambda_{e}^{2}\frac{\partial^{3}(\delta\tilde{B}_{y})}{\partial t\partial x^{2}} - 2ik_{0z}v_{te}^{2}\frac{\partial^{3}(\delta\tilde{B}_{y})}{\partial x^{2}\partial z}$$

$$- v_{te}^{2}\lambda_{e}^{2}\frac{\partial^{4}(\delta\tilde{B}_{y})}{\partial x^{2}\partial z^{2}} - 2ik_{0x}v_{te}^{2}\lambda_{e}^{2}\frac{\partial^{3}(\delta\tilde{B}_{y})}{\partial x\partial z^{2}}$$

$$+ 4k_{0x}k_{0z}v_{te}^{2}\lambda_{e}^{2}\frac{\partial^{2}(\delta\tilde{B}_{y})}{\partial x\partial z} + v_{A}^{2}k_{0z}^{2}\frac{\delta n}{n_{0}}\left(1 - \frac{\omega^{2}}{\omega_{ci}^{2}}\right)\delta\tilde{B}_{y} = 0.$$
(36)

## 2.2. Ion Acoustic Wave Dynamics

In a spatially varying wave propagation, a nonlinear force known as ponderomotive force is generated. The ponderomotive force is a time averaged force that acts on charged particles in a nonuniform electromagnetic field. Within a nonuniform, inhomogeneous plasma medium, the combined influence of the ponderomotive force and Joule heating, generated from plasma currents, can induce modifications to the plasma density (Shukla et al. 1999). In both laboratory and space plasma environments, large amplitude KAWs lead to fluctuations in plasma density, manifesting as humps and dips aligned with the field (Gekelman 1999; Shukla & Stenflo 2000a, 2000). These studies focused on the fluctuations of particle density under the adiabatic approximation, wherein the density changes slowly over time relative to density fluctuations. Here, we are considering non-adiabatic variations of particle density under the influence of ponderomotive force represented by the ion acoustic wave dynamics. Let us consider ion acoustic waves propagating along the z-direction  $\mathbf{k} = k_{0z}\hat{z}$  with magnetic field  $\mathbf{B} = B_0 \hat{z} + \delta B_y \hat{y}$ . The linearized continuity and momentum equations are given respectively as

$$\frac{\partial(\delta n_s)}{\partial t} + n_{0s} \frac{\partial(\delta v_{sz})}{\partial z} = 0, \tag{37}$$

and

$$m_{s} \left( \frac{\partial (\delta v_{s})}{\partial t} + \delta v_{sz} \frac{\partial (\delta v_{s})}{\partial z} \right)$$

$$= q_{s} \left( \delta \mathbf{E} + \frac{\delta v_{s} \times (B_{0}\hat{z} + \delta B_{y}\hat{y})}{c} \right) - \frac{k_{B}T_{s}}{n_{0s}} \frac{\partial (\delta n_{s})}{\partial z} \hat{z}. \quad (38)$$

Here, only the first-order linearization in the continuity equation is used, but both the first-order and second-order linearizations are applied in the momentum equation. The second-order linearization is utilized to obtain the dynamics of the ion acoustic wave due to the ponderomotive effects of the pump KAWs. The ponderomotive force term is

$$F_{s} = \frac{q_{s}}{c} (\delta v_{s} \times \delta B_{y} \hat{y}) - m_{s} \delta v_{sz} \frac{\partial (\delta v_{s})}{\partial z}, \tag{39}$$

where the first term is the Lorentz force and the second term is the convective term. The parallel velocity components satisfy the following equation

$$m_s \frac{\partial(\delta v_{sz})}{\partial t} = q_s \delta E_z - \frac{k_B T_s}{n_{0s}} \frac{\partial(\delta n_s)}{\partial z} + F_{sz}, \tag{40}$$

where  $F_{sz} = \frac{q_s}{c}(\delta v_{sx} \delta B_y) - m_s \delta v_{sz} \frac{\partial}{\partial z} \delta v_{sz}$  is the parallel component of the ponderomotive force due to the pump KAW. Here, only the parallel ponderomotive force is significant because we consider ion acoustic waves propagating along the z-direction. By assuming the massless electrons, we can find out the parallel component of the electric field as

$$\delta E_z = -\frac{1}{e} \frac{k_{\rm B} T_e}{n_{\rm O_z}} \frac{\partial (\delta n_e)}{\partial z} + \frac{1}{e} F_{ez}. \tag{41}$$

Imposing the quasi-neutrality condition, i.e.,  $n_{0i} = n_{0e} \equiv n_0$  and  $\delta n_i = \delta n_e \equiv \delta n$ , the continuity Equation (37) implies that  $\delta v_{iz} = \delta v_{ez}$ , hereafter we denote this variable as  $\delta v_z$ . Substituting Equation (41) in Equation (38), we get

$$\frac{\partial(\delta v_z)}{\partial t} = -\frac{c_s^2}{n_0} \frac{\partial(\delta n)}{\partial z} + \left(\frac{F_{iz} + F_{ez}}{m_i}\right). \tag{42}$$

Differentiating Equation (37) w.r.t. "t," we get

$$\frac{\partial^2(\delta n)}{\partial t^2} + n_0 \frac{\partial^2(\delta v_z)}{\partial t \partial z} = 0. \tag{43}$$

Substituting Equation (42) into Equation (43), we get the equation for density fluctuations due to the ponderomotive force of the pump KAW as

$$\frac{\partial^2(\delta n)}{\partial t^2} + n_0 \frac{\partial}{\partial z} \left[ -\frac{c_s^2}{n_0} \frac{\partial(\delta n)}{\partial z} + \frac{F_{iz} + F_{ez}}{m_i} \right] = 0.$$
 (44)

We rewrite Equation (44) as

$$\left(\frac{\partial^2}{\partial t^2} - c_s^2 \frac{\partial^2}{\partial z^2}\right) \frac{\delta n}{n_0} = -\frac{\partial}{\partial z} \left(\frac{F_{iz} + F_{ez}}{m_i}\right). \tag{45}$$

Similarly, we can write the equation for  $\delta v_z$  as

$$\left(\frac{\partial^2}{\partial t^2} - c_s^2 \frac{\partial^2}{\partial z^2}\right) \delta v_z = \frac{\partial}{\partial t} (F_{iz} + F_{ez}). \tag{46}$$

We see that the wave Equation (46) involves the time derivative of the ponderomotive forcing term due to the pump KAWs instead of the spatial derivative that appears in the density fluctuation Equation (45). Let us evaluate the parallel components of this forcing term by substituting the velocity components of pump KAWs as given in Equations (4), (6), (7) and (9) and averaging the Lorentz and the convective terms over the pump KAW time period of  $2\pi/\omega$  (Shukla & Stenflo 2000).

$$F_{z} = F_{ez} + F_{iz}$$

$$\simeq -\frac{e^{2}}{4\omega^{2}m_{e}}\frac{\partial}{\partial z}|\delta E_{z}|^{2} + \frac{e^{2}}{4m_{i}(\omega_{ci}^{2} - \omega^{2})}\frac{\partial}{\partial z}|\delta E_{x}|^{2}$$

$$+ \frac{e^{2}}{4m_{i}(\omega_{ci}^{2} - \omega^{2})}\frac{\partial}{\partial z}|\delta E_{y}|^{2}.$$
(47)

Now, let us evaluate the expressions for the perturbed electric fields to be substituted in Equation (47). From Equation (23), we get

$$\delta E_z = \frac{c\omega k_{0x}}{\omega_{pe}^2} \delta B_y. \tag{48}$$

From Equation (26) and (27) we obtain,

$$\delta E_{y} = \frac{\beta}{2} (ik_{0z}) \frac{c\omega_{ce}}{\omega_{pe}^{2}} \delta B_{y}. \tag{49}$$

Using Equations (26) and (27) in Equation (25), we arrive at

$$\delta E_x = \frac{\lambda_e k_{0z} \omega_{ce} \omega_{ci}}{\omega \omega_{pe}} \left[ \left( 1 - \frac{\omega^2}{\omega_{ci}^2} \right) - \frac{\beta}{2} \right] \delta B_y.$$
 (50)

Substituting Equation (47) into Equation (45) along with Equations (48), (49) and (50) and taking the magnetic field perturbations ( $\delta B_y$ ) as a plane wave modulated by a slowly varying envelope  $\delta \tilde{B}_y$  as previously defined in Equation (35), we get

$$\left(\frac{\partial^{2}}{\partial t^{2}} - c_{s}^{2} \frac{\partial^{2}}{\partial z^{2}}\right) \delta n = -\frac{e^{2} n_{0}}{4 m_{e} m_{i}} \frac{c^{2} k_{0x}^{2}}{\omega_{pe}^{4}} \left[ \frac{\left[ (1 - \omega^{2} / \omega_{ci}^{2}) - \beta \right]^{2}}{\lambda_{e}^{2} k_{0x}^{2} (1 - \omega^{2} / \omega_{ci}^{2})} - \frac{m_{i}}{m_{e}} \frac{k_{0z}^{2}}{k_{0x}^{2}} \frac{\beta^{2}}{(1 - \omega^{2} / \omega_{ci}^{2})} \right] \frac{\partial^{2}}{\partial z^{2}} |\delta \tilde{B}_{y}|^{2}.$$
(51)

Normalizing the pump KAW dynamical Equation (36) and the ion acoustic wave Equation (51), we get the following set of

equations

$$i\frac{\partial(\delta B_{y})}{\partial t} + i\frac{\partial(\delta B_{y})}{\partial x} + c_{1}\frac{\partial^{2}(\delta B_{y})}{\partial x^{2}} + c_{2}\frac{\partial^{2}(\delta B_{y})}{\partial z^{2}} + i\frac{\partial(\delta B_{y})}{\partial z} + c_{3}\frac{\partial^{2}(\delta B_{y})}{\partial t\partial x} - ic_{4}\frac{\partial^{3}(\delta B_{y})}{\partial t\partial x^{2}} - ic_{5}\frac{\partial^{3}(\delta B_{y})}{\partial x^{2}\partial z} - c_{6}\frac{\partial^{4}(\delta B_{y})}{\partial x^{2}\partial z^{2}} - ic_{7}\frac{\partial^{3}(\delta B_{y})}{\partial x\partial z^{2}} + c_{8}\frac{\partial^{2}(\delta B_{y})}{\partial x\partial z} + (1 - \omega^{2}/\omega_{ci}^{2})(\delta n)(\delta B_{y}) = 0$$
 (52)

and

$$\frac{\partial^2(\delta n)}{\partial t^2} - c_9 \frac{\partial^2(\delta n)}{\partial z^2} = -\frac{\partial^2(|\delta B_y|^2)}{\partial z^2}.$$
 (53)

Here, we have denoted  $\delta \tilde{B}_y$  as  $\delta B_y$  by removing the mark  $\sim$  placed on top of  $\delta B_y$  for the sake of writing.

The dimensionless parameters that appeared above are: 
$$c_1 = \frac{v_r^2 \lambda_e^2 k_{0z}^2 - \lambda_e^2 \omega^2}{v_A^2 k_{0z}^2 x_n^2}, c_2 = \frac{v_e^2 \lambda_e^2 k_{0x}^2 + c B_0 \beta \omega_{ci} / 8 \pi n_0 e + v_A^2 (1 - \omega^2 / \omega_{ci}^2)}{v_A^2 k_{0z}^2 z_n^2}, c_3 = \frac{4 \lambda_e^2 \omega k_{0x}}{v_A^2 k_{0z}^2 t_n x_n}, c_4 = \frac{2 \lambda_e^2 \omega}{v_A^2 k_{0z}^2 t_n x_n^2}, c_5 = \frac{2 k_{0z} v_{te} \lambda_e^2}{v_A^2 k_{0z}^2 x_n^2 z_n}, c_6 = \frac{v_{te}^2 \lambda_e^2}{v_A^2 k_{0z}^2 x_n^2 z_n^2}, c_7 = \frac{2 k_{0x} v_{te}^2 \lambda_e^2}{v_A^2 k_{0z}^2 x_n z_n^2}, c_8 = \frac{4 k_{0x} k_{0z} v_{te}^2 \lambda_e^2}{v_A^2 k_{0z}^2 x_n z_n}, and c_9 = \frac{c_s^2 t_n^2}{z_n^2}.$$
The normalizing parameters are: 
$$t_n = \frac{2 \omega (1 + \lambda_e^2 k_{0x}^2)}{v_A^2 k_{0z}^2}, c_8 = \frac{4 k_{0x} k_{0z} v_{te}^2 \lambda_e^2}{v_A^2 k_{0z}^2 x_n z_n}, c_8 = \frac{4 k_{0x} k_{0z} v_{te}^2 \lambda_e^2}{v_A^2 k_{0z}^2 x_n z_n}, c_8 = \frac{4 k_{0x} k_{0z} v_{te}^2 \lambda_e^2}{v_A^2 k_{0z}^2 x_n z_n}, c_8 = \frac{4 k_{0x} k_{0z} v_{te}^2 \lambda_e^2}{v_A^2 k_{0z}^2 x_n z_n}, c_8 = \frac{4 k_{0x} k_{0z} v_{te}^2 \lambda_e^2}{v_A^2 k_{0z}^2 x_n z_n}, c_8 = \frac{4 k_{0x} k_{0z} v_{te}^2 \lambda_e^2}{v_A^2 k_{0z}^2 x_n z_n}, c_8 = \frac{4 k_{0x} k_{0z} v_{te}^2 \lambda_e^2}{v_A^2 k_{0z}^2 x_n z_n}, c_8 = \frac{4 k_{0x} k_{0z} v_{te}^2 \lambda_e^2}{v_A^2 k_{0z}^2 x_n z_n}, c_8 = \frac{4 k_{0x} k_{0z} v_{te}^2 \lambda_e^2}{v_A^2 k_{0z}^2 x_n z_n}, c_8 = \frac{4 k_{0x} k_{0z} v_{te}^2 \lambda_e^2}{v_A^2 k_{0z}^2 x_n z_n}, c_8 = \frac{4 k_{0x} k_{0z} v_{te}^2 \lambda_e^2}{v_A^2 k_{0z}^2 x_n z_n}, c_8 = \frac{4 k_{0x} k_{0z} v_{te}^2 \lambda_e^2}{v_A^2 k_{0z}^2 x_n z_n}, c_8 = \frac{4 k_{0x} k_{0z} v_{te}^2 \lambda_e^2}{v_A^2 k_{0z}^2 x_n z_n}, c_8 = \frac{4 k_{0x} k_{0z} v_{te}^2 \lambda_e^2}{v_A^2 k_{0z}^2 x_n z_n}, c_8 = \frac{4 k_{0x} k_{0z} v_{te}^2 \lambda_e^2}{v_A^2 k_{0z}^2 x_n z_n}, c_8 = \frac{4 k_{0x} k_{0z} v_{te}^2 \lambda_e^2}{v_A^2 k_{0z}^2 x_n z_n}, c_8 = \frac{4 k_{0x} k_{0z} v_{te}^2 \lambda_e^2}{v_A^2 k_{0z}^2 x_n z_n}, c_8 = \frac{4 k_{0x} k_{0z} v_{te}^2 \lambda_e^2}{v_A^2 k_{0z}^2 x_n z_n}, c_8 = \frac{4 k_{0x} k_{0z} v_{te}^2 \lambda_e^2}{v_A^2 k_{0z}^2 x_n z_n}, c_8 = \frac{4 k_{0x} k_{0z} v_{te}^2 \lambda_e^2}{v_A^2 k_{0z}^2 x_n z_n}, c_8 = \frac{4 k_{0x} k_{0z} v_{te}^2 \lambda_e^2}{v_A^2 k_{0z}^2 x_n z_n}$$

$$x_n = \frac{2(v_{te}^2 \lambda_e^2 k_{0z}^2 k_{0x} - k_{0x} \lambda_e^2 \omega^2)}{v_A^2 k_{0z}^2}, \quad z_n = \frac{2k_{0z} \left[ v_{te}^2 \lambda_e^2 k_{0x}^2 + \frac{cB_0 \beta \omega_{ci}}{8\pi n_0 e} + v_A^2 \left( 1 - \frac{\omega^2}{\omega_{ci}^2} \right) \right]}{v_A^2 k_{0z}^2},$$

$$n_n = n_0 \text{ and } B_n = \left( \frac{z_n^2 n_n m_i \omega_{pe}^4}{M t_n^2 \omega^2 c^2 k_{0x}^2} \right)^{1/2}, \text{ where } M \text{ is a dimensionless}$$

parameter given by 
$$M = \frac{n_0 e^2}{4m_e \omega^2} \left[ \frac{(1 - \omega^2 / \omega_{ci}^2 - \beta)^2}{\lambda_e^2 k_{0x}^2 (1 - \omega^2 / \omega_{ci}^2)} - \frac{m_i k_{0x}^2}{m_e k_{0x}^2} \frac{\beta^2}{1 - \omega^2 / \omega_{ci}^2} \right].$$

### 3. Numerical Simulation

Equations (52) and (53) constitute modified ZSEs describing the nonlinear coupling between pump KAWs (dispersive) and ion acoustic waves (approximately non-dispersive). In the adiabatic limit, this system of equations becomes the modified Nonlinear Schrödinger Equation (NLSE) with the substitution of density perturbation as  $\delta n \propto |\delta B_v|^2$ . We performed a numerical simulation of the modified ZSEs using the pseudospectral method where the spatial derivatives can be calculated using orthogonal functions such as Fourier integrals, Chebyshev polynomials, etc. In our simulation, we used the Fourier integrals evaluated via Fast Fourier Transform, thereby converting the space derivatives into the wavenumber domain by multiplication of the spectrum with ik where k is the wavenumber. The inverse Fourier Transform gives the exact space derivative up to the Nyquist frequency. The spatial integration was carried out on  $2^7 \times 2^7$  grid points with a periodic domain of dimensions  $L_x = \frac{2\pi}{\alpha_x}$  and  $L_z = \frac{2\pi}{\alpha_z}$ , where  $\alpha_x$ and  $\alpha_z$  represent the perturbation wavenumbers in the x and z directions normalized by  $x_n^{-1}$  and  $z_n^{-1}$  respectively. The temporal first derivative was evaluated in Fourier space using Newton's forward difference with a step size of  $dt = 5 \times 10^{-5}$ and then the leap-frog time step method and predictor-corrector method. Such difference approximations to differential equations are accurate when the wavenumbers are low enough. As the wavenumbers increase, the linear terms dominate the nonlinear terms in the differential equation, hence reducing the accuracy. To circumvent this, we modified the linear terms in the leap-frog step using the ideas of Fornberg and Withham (Fornberg & Whitham 1978). On the other hand, if we calculate the nonlinear terms directly in Fourier space it leads to the convolution involving  $N^2$  operations for quadratic nonlinearity, where N is the number of grid points. In case of higher nonlinearity, the situation gets even worse involving more operations. To overcome this problem, instead of evaluating the nonlinear terms in Fourier space directly, we transformed the involved variables back to real space and evaluated the nonlinearity in real space and then in Fourier space. With this procedure the number of operations involved in quadratic nonlinearity is reduced to  $N \log N$ , yielding fast computational speed.

We first developed an algorithm to solve 2D-cubic NLSE and compared the results with other available results. The NLSE is an important and well-known model of nonlinear phenomena in fluids and plasmas. To test the numerical code, we set the benchmark of the algorithm by calculating the conservation of the plasmon number given by

$$P = \frac{1}{L_x} \frac{1}{L_z} \int_0^{L_x} \int_0^{L_z} |\delta B_y|^2 dx dz$$
  
= 
$$\int_{-\infty}^{\infty} \int_{-\infty}^{\infty} |\delta B_{yk}|^2 dk_x dk_z = \sum_k |\delta B_{yk}|^2,$$

which is conserved up to the accuracy of  $10^{-6}$ . The same code was modified for the modified ZSEs of our problem which is nonintegrable. On the other hand, the discrete Fourier transform of a periodic function introduces the so called aliasing error at each time step simulated with finite grid resolution when the nonlinear interactions are not fully resolved in the fixed computational grids. In the quadratic nonlinear term, the aliasing errors occur when the addition of the wavenumbers  $(k_1 + k_2)$  exceeds the Nyquist sampling criterion, i.e.,  $(k_1 + k_2) > N$  where  $k_1, k_2 \in \left[ -\frac{N}{2} + 1, \frac{N}{2} \right]$ , and N is the number of equidistant discrete points in spatial directions. In our simulation, we used a phase shift dealiasing scheme which is described here briefly for the sake of completeness. In evaluating the nonlinear term  $(f_ig_i)$  of variables f and g at grid points j = 0, 1, ..., (N-1), the dealiasing operation is performed by taking the Fourier transform at the shifted grid points. The variables f and g at real space are represented as

Radiation Belt Streamer Belt Radiation Belt Streamer Belt  $2.04 \times 10^{6} \, \text{cm}$  $1.34 \times 10^6 \, \text{cm}$ 0.93436342 0.00049027  $\rho_i$  $c_1$  $6.5 \times 10^{5} \, \text{cm}$  $1.90 \times 10^{6} \, \text{cm}$ 0.19143023 0.00048930  $c_2$  $\rho_s$  $4.877 \times 10^8 \, \mathrm{cm \ s^{-1}}$  $3.45 \times 10^6 \, \mathrm{cm \ s^{-1}}$ 0.14374822 0.00007543  $v_{A}$  $c_3$  $9.785 \times 10^7 \, cm \; s^{-1}$  $6.42 \times 10^6 \, cm \ s^{-1}$ 0.13431308 0.00000004  $C_{\varsigma}$  $C_4$  $1.349 \times 10^9 \, cm \ s^{-1}$  $3.89\times 10^8\,cm\;s^{-1}$ 0.81813534 0.00000096  $v_{te}$ C5  $2.005\times 10^{-9}\,\text{cm}^{-1}$  $5.99\times 10^{-8}\,cm^{-1}$  $k_{0z}$  $c_6$ 0.15661584 0.00000000  $8.416 \times 10^{-7} \, \text{cm}^{-1}$  $1.19 \times 10^{-5} \, \text{cm}^{-1}$ 0.16761769 0.00000096  $k_{0x}$  $c_7$  $6.359 \times 10^{5} \, \text{cm}$  $8.57 \times 10^{7} \, \text{cm}$ 0.87560720 0.00195724  $c_8$  $1.71 \times 10^{10} \text{ cm}$  $1.302 \times 10^{9} \, \text{cm}$ 0.02451409 0.00000310  $z_n$  $C_{0}$ 2.084 s4.67 s $t_n$  $1.286 \times 10^{-2} \,\mathrm{G}$  $4.013 \times 10^{-2} \, G$ . . .  $B_n$ 

Table 1
Simulation Parameters for Radiation Belt and Near-Sun Streamer Belt Solar Wind

(Yin et al. 2005; Sinhababu & Ayyalasomayajula 2021)

$$f_j^s = \sum_{|k| \leq \frac{N}{2}} \hat{f} e^{i(x_j + \Delta)}, \tag{54}$$

$$g_j^s = \sum_{|k| \le \frac{N}{2}} \hat{g}e^{i(x_j + \Delta)},\tag{55}$$

where  $x_j$  is the collocation points and the superscript s denotes the variables in the shifted grids. The next step is the multiplication of these variables in the shifted grid as

$$\mathcal{NL}_{i}^{s} = f_{i}^{s}.g_{i}^{s}. \tag{56}$$

Fourier transform of the nonlinear terms on the shifted grids is obtained as

$$\widehat{\mathcal{NL}^s} = \frac{1}{N} \sum_{i=0}^{N-1} \mathcal{NL}_j^s e^{-i(x_j + \Delta)}.$$
 (57)

It can be expressed as (Patterson & Orszag 1971; Canuto et al. 2007; Kopriva 2009)

$$\widehat{\mathcal{NL}^s} = \sum_{p+q=k} \hat{f}_p \hat{g}_q + e^{\pm iN\Delta} \left( \sum_{p+q=k\pm N} \hat{f}_p \hat{g}_q \right).$$
 (58)

Taking  $\Delta = \pi/N$ , the nonlinear terms free from aliasing error are obtained as (Canuto et al. 2007)

$$\widehat{\mathcal{NL}} = \frac{1}{2} \left( \widehat{\mathcal{NL}}^s + \sum_{p+q=k} \hat{f}_p \hat{g}_q \right).$$
 (59)

Since the linear evolution in the differential equation is exactly integrable, a plane wave solution is a possible solution. We used a uniform plane pump KAW of fixed amplitudes superimposed by a sinusoidal periodic perturbation as the initial condition of the simulation as

$$\delta B_{y}(x, z, t = 0) = \delta B_{y0}[1 + \epsilon \cos(\alpha_{x}x)] \times [1 + \epsilon \cos(\alpha_{z}z)],$$
(60)

where  $\epsilon$  represents the magnitude of the perturbation and  $\delta B_{y0}$  is the amplitude of the pump KAW. Although the magnetic

waves in astrophysical plasmas are more complicated, they can be represented as the sum of the sinusoidal wave components.

The initial condition of the density perturbation was taken as

$$\delta n = |\delta B_{\nu}|^2. \tag{61}$$

The modified ZSEs (52) and (53) were simulated for two different regions based on the plasma  $\beta$  values (a) the Earth's radiation belt ( $\beta$  < 1) and (b) near-Sun streamer belt solar wind ( $\beta$  > 1) at distance of  $\approx$ 0.13–0.25 au from the surface of the Sun. In the simulation, we used  $\delta B_{y0} = 1$ ,  $\epsilon = 0.1$ , and  $\alpha_x = \alpha_y = 0.01$ . The plasma parameters chosen for the radiation belt are (Cattell et al. 2008; Goyal et al. 2018):  $B_0 \approx 5.0 \times 10^{-3} \, \text{G}$ ,  $n_0 \approx 5.0 \, \text{cm}^{-3}$ ,  $T_e \approx 6.0 \times 10^6 \, \text{K}$  and  $T_i \approx 1.1 \times 10^8 \, \text{K}$ . Employing these values, the other parameters are calculated as  $\beta \approx 4.16 \times 10^{-3}$ ,  $w_{ce} \approx 8.8 \times 10^4 \, \text{s}^{-1}$ ,  $w_{ci} \approx 47.9 \, \text{s}^{-1}$ ,  $\omega_{pe} \approx 1.261 \times 10^5 \, \text{s}^{-1}$  and  $\lambda_e \approx 2.37 \times 10^5 \, \text{cm}$ . We used  $\omega/\omega_{ci} = 0.02$  for a finite frequency and  $k_{0x}\lambda_e = 0.2$ . Accordingly, we calculated other parameters and the normalizing parameters corresponding to the radiation belt, which are tabulated in Table 1.

The plasma parameters chosen for the near-Sun streamer belt solar wind that were taken from the fourth orbit of the PSP when it reaches around 28–54 solar radii (Chen et al. 2021a; Liewer et al. 2023) are:  $B_0 \approx 5.0 \times 10^{-4} \, \mathrm{G}$ ,  $n_0 \approx 10^3 \, \mathrm{cm}^{-3}$  and  $T_e \approx 5.0 \times 10^5 \, \mathrm{K}$ . Employing these values, the other parameters are calculated as  $\beta \approx 6.94$ ,  $w_{ce} \approx 8.79 \times 10^3 \, \mathrm{s}^{-1}$ ,  $w_{ci} \approx 4.79 \, \mathrm{s}^{-1}$ ,  $\omega_{pe} \approx 1.78 \times 10^6 \, \mathrm{s}^{-1}$  and  $\lambda_e \approx 1.68 \times 10^4 \, \mathrm{cm}$ . We used  $\omega/\omega_{ci} = 0.02$  for a finite frequency and  $k_{0x}\lambda_e = 0.2$ . Accordingly, we calculated other parameters and the normalizing parameters corresponding to the near-Sun streamer belt solar wind, which are tabulated in Table 1.

We analyze here the numerical results of the modified ZSEs applicable to the Earth's radiation belt. First, the magnetic field intensity profiles of KAWs in the form of generation of filaments are shown in Figure 1 at six different instants of normalized times (t = 0.5, 13, 18, 44, 75, and 95). It is evident from the figure that the magnetic field intensities are localized in space with periodic patterns initially and with the evolution

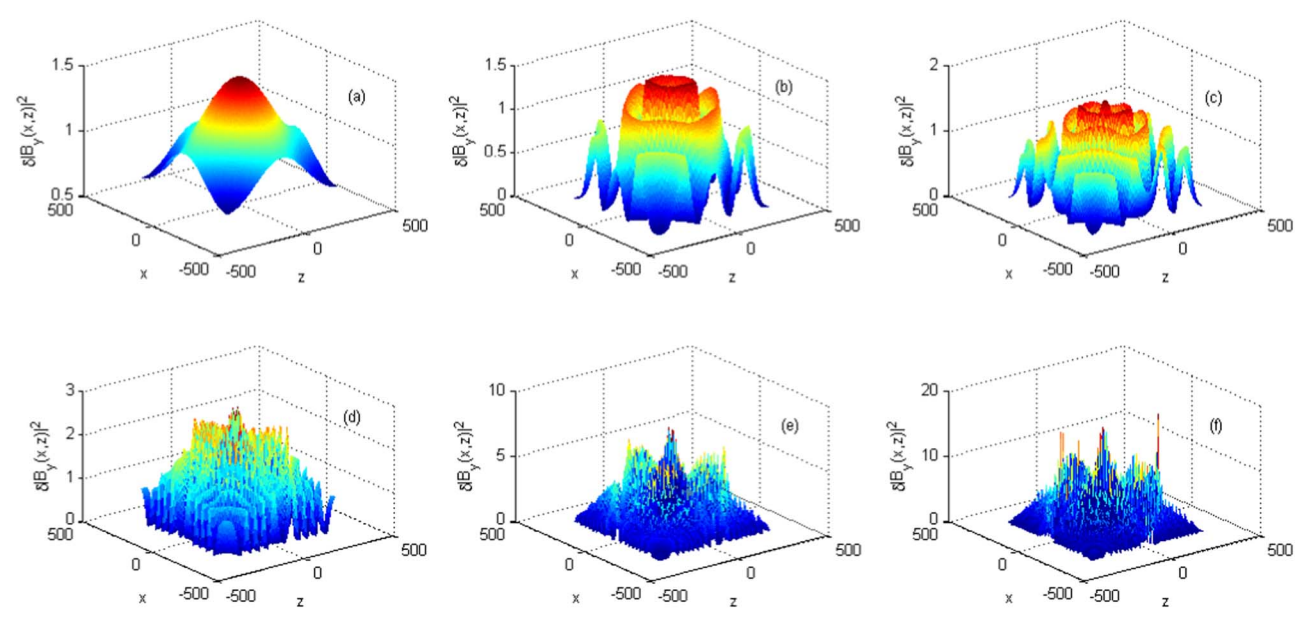


Figure 1. Snapshots of fluctuating magnetic field intensity profiles of KAWs at (a) t = 0.5, (b) t = 13, (c) t = 18, (d) t = 44, (e) t = 75 and (f) t = 95.

of time, they change to quasi-periodic and chaotic structures. The nonlinear ponderomotive force exerted by the pump KAW induces the background density variations, leading to changes in the phase velocity of KAWs. The changes in the phase velocity result in the spatial localization of KAWs in the x-zplane. In astrophysical plasma, the process of magnetic coherent (localized) structure generation of waves is the same as that of laser beam filamentation in laboratory plasma. When a high-power laser beam propagates through plasma, the associated ponderomotive force modifies the plasma density, thereby varying the refractive index of the medium. In this way, the medium acts as a converging lens, producing a focused laser beam. In a similar way, when KAWs propagate through astrophysical plasma, the parallel ponderomotive force acting on the plasma will produce variations in the density resulting in varying phase velocity. This will generate spatial localization of KAWs having coherent structures. As time evolves, the perturbations associated with the pump KAWs take the magnetic energy leading to the collapse of the magnetic coherent structures. However, due to the nonlinear interactions of magnetic field and density, these collapsed structures try to regroup as time advances. These structures become more intense and chaotic with the advancement of time, reaching the highest amplitude as well as a more chaotic distribution at t = 95, as shown in Figure 1(f). Beyond this time, we cannot see any significant changes in the magnetic field intensity profiles as the modulational instability saturates. It means at t = 95, the system reaches a quasi-steady state. Although the evolution of the magnetic field coherent structures is dependent on the initial conditions and the nonlinearities involved, once

the quasi-steady state is reached, the system is no more dependent on these conditions. The transverse scale size of the localized magnetic filaments at t = 0.5, 13 and 18, as shown in Figure 1(a)–(c), is of the order of ion gyroradius or ion inertial length which is the energy injection scale, whereas it is electron gyroradius or electron inertial length for t = 44, 75 and 95 as shown in Figure 1(d)–(f) which is the energy dissipation scale. In the collapsed magnetic structures or density gradient regions, large parallel electric fields are generated that can accelerate the electrons along the direction of the background magnetic field (Génot et al. 2000; Tsiklauri 2012). At sufficiently large fluctuations in the parallel fields and the current densities, the electrons can be trapped in between the wave packets (filaments) (Gershman et al. 2017). As the waves propagate, their kinetic energy is converted to particle energy, the process that can be considered as a magnetic analog of Landau damping. If the size of the wave packets is smaller than the ion thermal gyroradius  $\rho_i$ , the ion motion decouples from the electron motion. From the fluctuating magnetic intensity profiles, we found that in the early stages of magnetic field evolution, the size of the transverse filaments is of the order of the ion thermal gyroradius ( $\approx 6\rho_i \approx 10^4$  km) at half of the intensity peak as also observed by Lion et al. (2016) and Passot et al. (2014). As the system evolves, these filamentary structures undergo a transverse collapse, significantly reducing their size to less than the characteristic length scale  $\rho_i$ . When the size of the filaments reaches the kinetic scale comparable to the short perpendicular wavelength of KAWs, the energization of plasma particles can happen through wave-particle energy exchange.

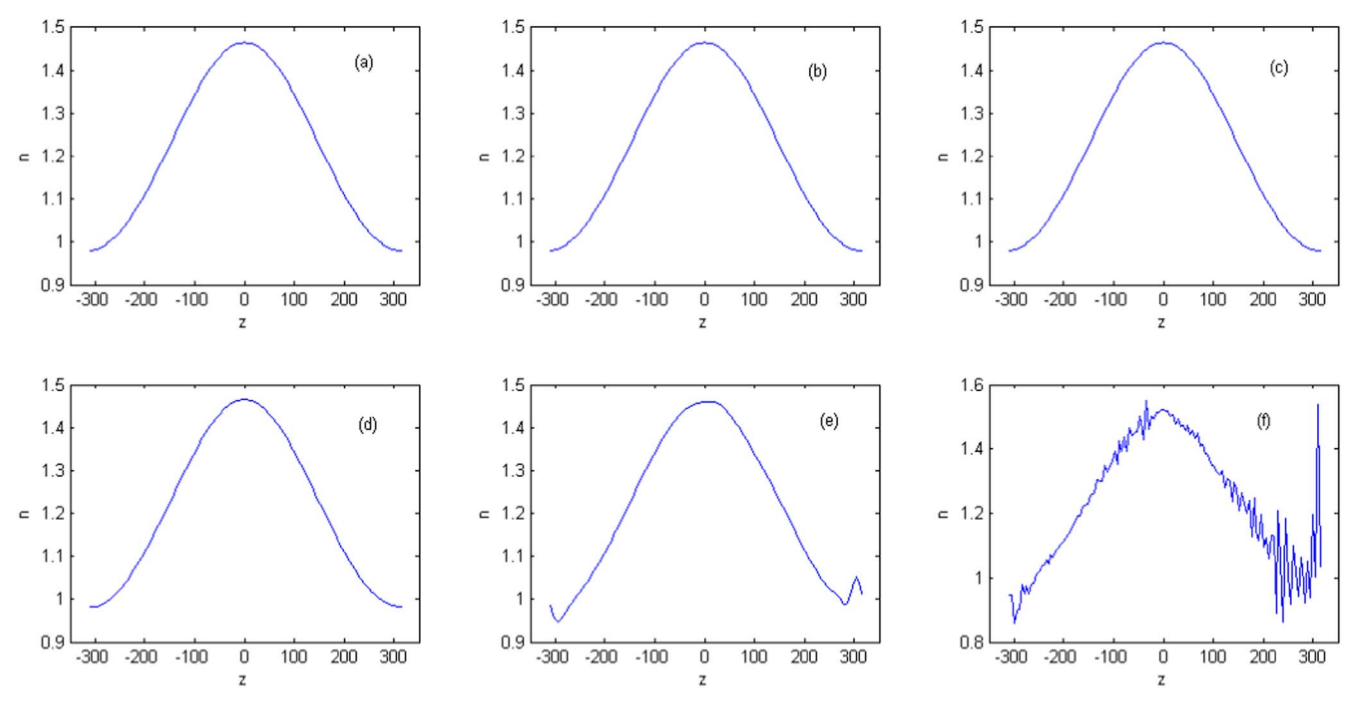


Figure 2. Density fluctuations along the z-direction at different times applicable for the Earth's radiation belt: (a), (b), (c), (d), (e) and (f) correspond to the density fluctuations at times t = 0.5, 13, 18, 44, 75, and 95 respectively.

Figure 2 depicts density fluctuations along the z-direction at different times applicable for the Earth's radiation belt corresponding to Figure 1. Before the turbulent state, density cavitons (humps) are formed (Figure 2(a)–(d)). Because of the ponderomotive force, the magnetic field is trapped in the regions of density cavities producing magnetic coherent structures. However, as the perturbation associated with the pump KAW takes the magnetic energy, the magnetic coherent structures tend to collapse. Due to the nonlinear interactions of magnetic field and density, these collapsed structures try to regroup as time advances. Therefore, we can see only density cavitons (humps) and no density depletions until t = 44(Figure 2(d)) before the turbulent state was set. In Figure 2(e) we can see small density depletions at  $z \approx \pm 300$ where the system starts to be in a chaotic state. In Figure 2(f) when the system reaches the quasi-steady turbulent state, many density humps and depletions are observed. One can study the phenomenon of turbulence by examining the cascading of energy and the process of density cavitation through ZSEs as suggested by Doolen et al. (1985). They suggested that Langmuir waves are localized when the wave packets are trapped in density cavities. Also, Sharma et al. (1996) studied the Langmuir turbulence by energy cascades and cavitation process.

It is worth mentioning here that ion acoustic waves generate solitons with density humps in electron-ion plasma (Davidson 2012). In electron-positron-ion plasma, the amplitudes of the

ion acoustic waves will be reduced, producing density dips depending on the strength of the positron concentrations (Popel et al. 1995). A similar method of producing density humps and dips was also reported in the case of KAWs. Many decades ago, Hasegawa & Mima (1976) predicted that density humps would be produced when KAWs propagate in electron-ion plasma at the sub-Alfvénic regime. In the super-Alfvénic regime, the KAWs produce density dips in electron-positronion plasma (Saleem & Mahmood 2003). Similar results were also obtained by studying the nonlinear KAWs in dusty plasma (Yinhua et al. 2000) and quantum magnetoplasma (Sadiq et al. 2018). However, all these studies did not consider the coupling of ion acoustic waves with KAWs when the effect of ion inertia in parallel motion is taken into account.

In order to analyze the evolution of the magnetic field in Fourier modes, we plotted  $|\delta B_{yk}|$  as a function of t (Figure 3) across three distinct modes: Mode A  $(k_x=1,\,k_z=0)$ , Mode B  $(k_x=2,\,k_z=0)$  and Mode C  $(k_x=3,\,k_z=0)$  where  $k_x$  and  $k_z$  are wavenumbers of KAWs generated by the interaction of pump KAWs (having wavenumbers  $k_{0x}$  and  $k_{0z}$ ) and ion acoustic waves propagating in an inhomogeneous plasma medium. It is observed from the figure that the major participants in the energy sharing process are mostly confined to low wavenumber modes. Mode A has the maximum share of energy at initial time, but it decays with time sharing its energy with other higher modes B and C showing an oscillatory evolution.

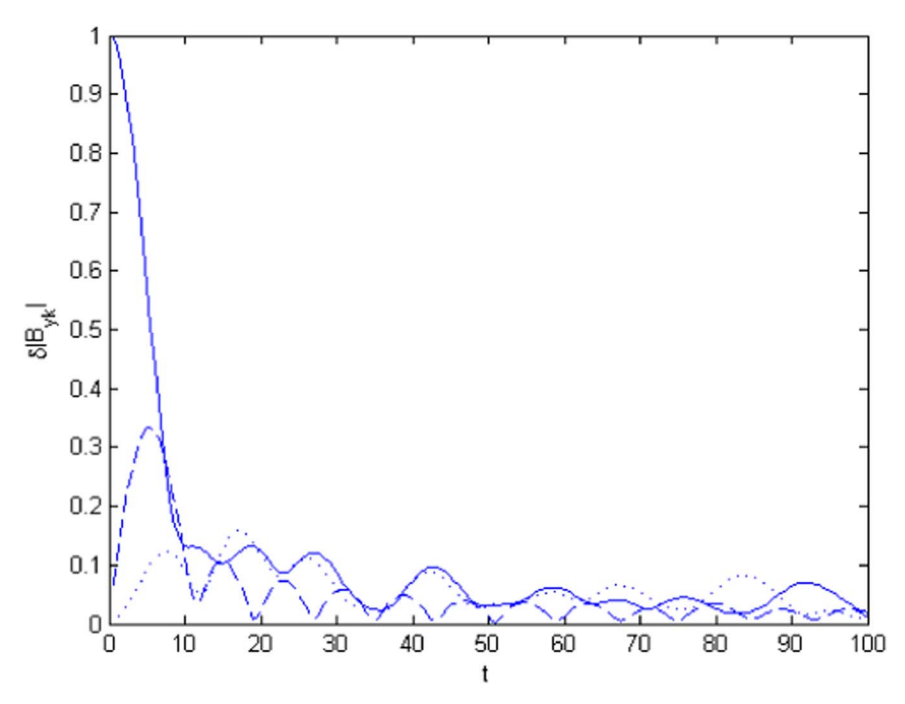


Figure 3. Evolution of the magnetic field in Fourier mode across three distinct modes: Mode A (solid line with  $k_x = 1$ ,  $k_z = 0$ ), Mode B (dashed line with  $k_x = 2$ ,  $k_z = 0$ ) and Mode C (dotted line with  $k_x = 3$ ,  $k_z = 0$ ).

To study the distribution of magnetic energy across various wavenumbers, we plotted  $|\delta B_{vk}|^2$  against  $k_x(k_{\perp})$  represented by Figure 4. At t = 0.5, only a single wave mode exists, but higher harmonics are generated at later times. Initially, magnetic energy is concentrated in low wavenumber modes, but it becomes distributed across higher wavenumber modes as time progresses. Further, to understand more about the turbulent behavior of the magnetic field in radiation belt plasma, we examined the fluctuating magnetic field spectrum  $|\delta B_{vk}|^2$  versus  $k_{\perp}$  (averaged over  $k_{\parallel}$ ) plotted at t = 95 (Figure 5) when the turbulence reaches the quasi-steady state. It is evident that for scales larger than ion inertial length  $(k_{\perp}\rho_i < 1)$  known as the inertial range created by the energy conserving spectral cascade (Smith et al. 2006), the fluctuating magnetic spectrum approaches the Kolmogorov scaling with a spectral index of -5/3 (i.e.,  $|\delta B_{\nu k}|^2 \propto k_{\perp}^{-5/3}$ ). In the inertial regime, fluid dynamics can still be used to study the interactions between fluctuations. In many solar and magnetospheric plasmas, the Kolmogorov spectral index of -5/3 (Shaikh & Zank 2009; Borovsky 2012; Xu et al. 2023) as well as the Iroshnikov-Kraichnan spectral index of -3/2 (Smith et al. 2006; Podesta 2011; Zhao et al. 2022a) has been reported. Beyond this range, steepening in the magnetic field power spectrum occurs as such individual particle effects and thermal heating take over (Leamon et al. 1998; Smith et al. 2006; Alexandrova et al. 2008; Lion et al. 2016) which is regarded as dissipation range. From the power spectrum (Figure 5) we can see that the

first spectral break appears at  $k_{\perp}\rho_i \approx 0.76$  which corresponds to the transition from the inertial range (ion scale) to the kinetic range (electron scale). For  $k_{\perp}\rho_i > 0.76$  the spectral index is much steeper which is  $\sim -3$ . By analyzing the Van Allen Probes' observations, Moya et al. (2015) reported magnetic frequency power spectral indices of -1.1 to -1.7 for frequency  $\gtrsim$ 2 Hz (inertial range) and -4 to -5 for frequency  $\lesssim$ 2 Hz (subkinetic scale) that are consistent with weak KAW turbulence. Some authors (Markovskii et al. 2006; Bruno & Trenchi 2014; Lion et al. 2016) have also reported varying spectral indices between -1 and -4, depending on turbulent fluctuations. The steepening of the spectral index is an indication that the transfer of energy from a larger scale (lower frequency) to a smaller scale (higher frequency) happens. This may be considered as one reason to accelerate the plasma particles, thereby increasing the plasma temperature. As the plasma particles take away some of the energy of the fluctuations, it leads to the energization of the plasma which could be the main reason for the steeper spectrum. The physical process involving the transition from inertial to dissipation range at ion-kinetic scales is still an ongoing inquiry (Bowen et al. 2020; Matteini et al. 2020; Terres & Li 2022).

We have also performed the numerical simulation of the modified ZSEs for  $\beta > 1$ , applicable for the parameters in the near-Sun streamer belt solar wind. The essential plasma and simulation parameters are given in the Table 1. The same trends of magnetic filament formation, regrouping and collapsing at later times happened. Since it has almost the same characteristics as

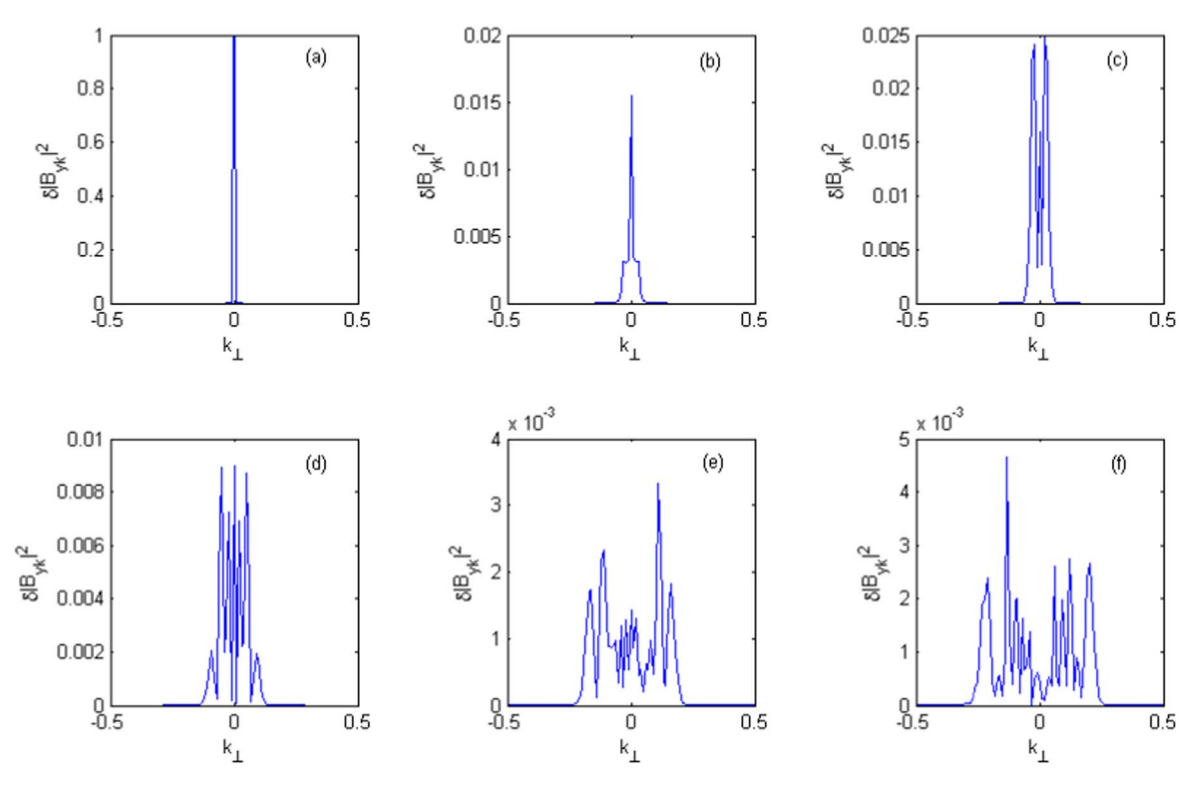


Figure 4. Distribution of magnetic energy across various wavenumbers at six different times: (a), (b), (c), (d), (e) and (f) with t = 0.5, 13, 18, 44, 75 and 95 respectively. Initially, at t = 0.5 only a single wave mode exists, but higher harmonics are generated at later times.

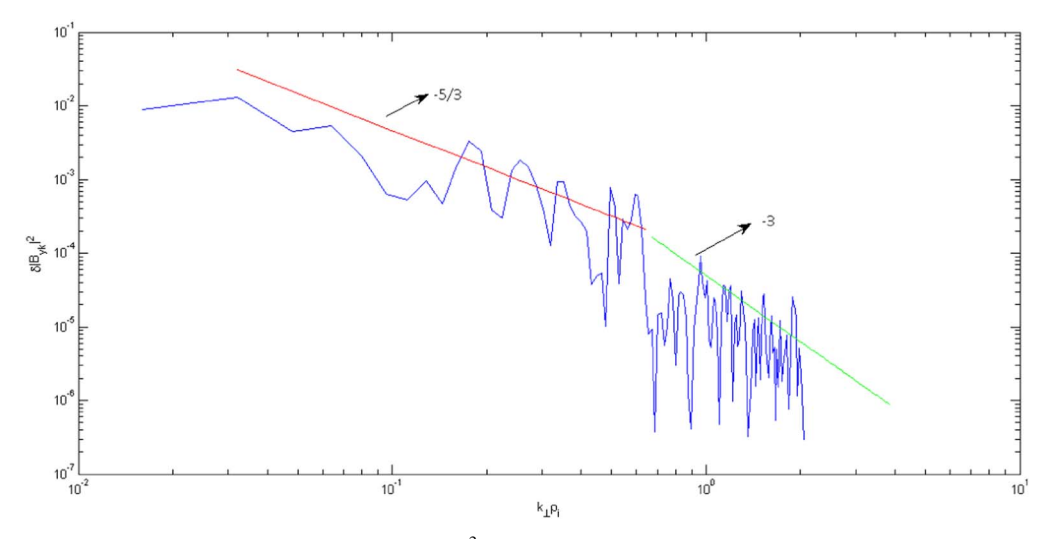


Figure 5. The fluctuating magnetic power spectrum  $|\delta B_{yk}|^2$  vs.  $k_{\perp}\rho_t$  plotted at t=95 for the Earth's radiation belt plasma,  $\beta<1$ .

that of the radiation belt corresponding to  $\beta$  < 1, instead of showing all the graphical results and analyzing them in detail, we are showing here the fluctuating magnetic field power spectrum plotted at t = 76 when the quasi-steady state is reached (Figure 6) and are reporting a few basic differences from the two regions. In

the case of near-Sun streamer belt solar wind, there is an increase in total magnetic power fluctuations and spectral break wavenumber  $(k_\perp \rho_i \approx 1)$  with a steeper spectral index of -4 in the dissipation range (Figure 6) in comparison to the -3 of the radiation belt region. In order to understand the spectral properties

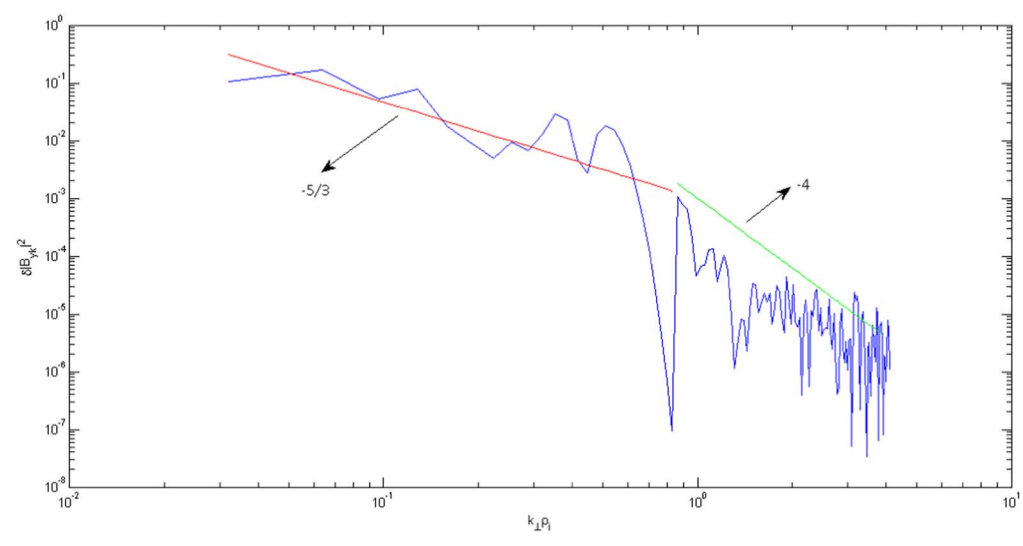


Figure 6. The fluctuating magnetic power spectrum  $|\delta B_{yk}|^2$  vs.  $k_{\perp}\rho_i$  plotted at t=76 for near-Sun streamer belt solar wind plasma,  $\beta>1$ .

of the magnetic field fluctuations in the inner heliosphere, many researchers (Lotz et al. 2023; Šafránková et al. 2023) carried out a statistical study on PSP and Solar Orbiter data at various distances from the Sun. Šafránková et al. (2023) found the inertial range spectral index of -3/2 at the closest approach (0.12 au) to the Sun, then becoming steeper as it moves away, reaching -5/3 at around 0.4 au. A similar trend of transition from -3/2 to -5/3when the solar wind passes from 0.17 to 0.60 au was also investigated by Chen et al. (2020). By analyzing the PSP magnetic field observations, Zhao et al. (2022b) reported a -5/3spectral index in the inertial region. In the dissipation range, it was -4.8 at the closest approach to the Sun then became more flat as it moved away, approaching  $\approx -3$  at around 0.4 au (Šafránková et al. 2023). From 0.4 to 1 au, the spectral indices remained approximately constant (-5/3) at inertial and  $\approx -3$  at dissipation range). Lotz et al. (2023) found the inertial range spectral index varied between -1.45 to -1.65 and the dissipation range spectral index varied between -4 at 0.1 au to -3 at 0.7 au. The steepening of the spectral index as the PSP moves toward the Sun can be attributed to the enhanced power of the turbulence with decreasing radial distance from the Sun (Smith et al. 2006; Bruno & Trenchi 2014; Huang et al. 2021). The increase of magnetic power fluctuations and spectral break wavenumber toward the Sun is expected (Lotz et al. 2023).

Many authors (Velli 2003; Wu et al. 2016; Malara et al. 2019; Nättilä & Beloborodov 2022) proposed that dissipation of Alfvén waves leading to turbulent energy cascade in high wavenumbers may be responsible for heating the astrophysical plasmas. They calculated the energy flux density in the coronal loops and found it to be consistent with the observational results. However, the physical mechanism behind this turbulent energy cascade has not been satisfactorily explained until now. The transverse collapse of KAWs via magnetic filaments may be considered as one of the

reasons to explain Kolmogorov turbulence and dissipation range heating. To sufficiently heat the solar corona by small-scale bursts such as solar flares, Hudson (1991) and others (Tu & Marsch 2001; Simnett 2005) found that the energy spectral index has to be much steeper than -2. Such kind of steep spectral index has also been pointed out in the quite-Sun and active regions by analyzing the observational data from many spacecraft such as Yohkoh with SXT, SOHO and TRACE (Phillips 2000; Aschwanden & Parnell 2002; Domingo 2002). It should be mentioned here that our present KAW model is valid for  $k_{\perp}\rho_{i}\lesssim 1$  because of the lowfrequency condition  $\omega < \omega_{ci}$ . For  $k_{\perp}\rho_i \gg 1$ , the waves at electron scales lead to Landau damping via wave-particle interactions (Gary & Nishimura 2004; Sahraoui et al. 2009; Bian et al. 2010). In this region, whistler mode  $\omega > \omega_{ci}$  may be more relevant. However, the origin of fluctuating turbulent spectra at small scales has not been properly resolved despite many studies suggesting it is due to different wave modes such as whistler waves, ion cyclotron waves, Alfvén cyclotron waves, KAWs, magnetosonic waves, ion acoustic waves or interactions among these waves (Dwivedi et al. 2012; Boldyrev et al. 2013; Chen et al. 2013; López et al. 2017; Singh & Jatav 2019b). Therefore, our present model of KAW dynamics coupled with density perturbations generated by ion acoustic waves due to the parallel ponderomotive force leading to the transverse collapse of the magnetic coherent structures may be one of the candidates to explain the physical process of turbulence and the particle heating in various astrophysical plasmas.

## 4. Particle Heating

The ion scale nature of KAWs was reported by Liu et al. (2023) when the KAW-ion decoupling is induced by the finite Larmor gyroradius effect at  $\rho_i \sim \lambda_{\perp}$ , where  $\lambda_{\perp}$  is the perpendicular wavelength of KAWs. Since the decoupling

happens at the energy corresponding to the local proton thermal energy  $(e^2B_0^2\rho_i^2/2m_p)$ , the bulk of the proton population is partially decoupled from the wave fields, providing evidence of KAW-particle interaction. By analyzing the Magnetospheric Multiscale (MMS) Mission data, Liu et al. (2023) determined statistically  $\lambda_{\perp} \approx (2.4 \pm 0.7) \rho_i$ . Some studies (Lysak et al. 1980; Chaston et al. 2004; Shen & Knudsen 2020) suggested that it is difficult for coherent wave-particle interactions to produce particles having gyroradius larger than the perpendicular wavelength  $(\lambda_{\perp})$  of the waves involved (i.e.,  $\sqrt{2m_p W_{\perp,m}}/eB_0 \lesssim \lambda_{\perp}$ ). This condition sets the maximum perpendicular energy that a proton can reach in coherent interactions with KAWs as  $W_{\perp,m} \lesssim e^2 B_0^2 \lambda_{\perp}^2 / 2m_p$ , that is, 5.76 (2.4<sup>2</sup>) times the proton perpendicular thermal energy (Liu et al. 2023). Although this limit applies on the majority of the proton population, few protons can attain energy higher than this restriction through the process of stochastic heating (Lysak et al. 1980; Chaston et al. 2004; Shen & Knudsen 2020).

When turbulent KAW amplitudes exceed a certain threshold, the proton motion perpendicular to the background magnetic field  $B_0$  becomes chaotic (Johnson & Cheng 2001; Chaston et al. 2004; Fiksel et al. 2009). The protons then interact stochastically with the time-varying electrostatic potential and proton energy can be reasonably approximated by a random walk. If a single proton performs a random walk in energy, it can gain or lose energy with the same probability during a time  $\Delta t$ . However, if the number of thermal protons (initially having isotropic Maxwellian distribution in velocity) is large, then they will gain more energy leading to stochastic proton heating (Hoppock et al. 2018). Using phenomenological arguments, the proton heating rates for low  $\beta$  plasma ( $\beta \ll 1$ ) and high  $\beta$ plasma ( $\beta \sim 1$ –30) were calculated at  $k_{\perp} \rho_i \sim 1$  by Chandran et al. (2010) and Hoppock et al. (2018) respectively. The repetitive interactions of charged particles with the collapsed magnetic structures can heat the particles via the second-order Fermi acceleration mechanism as explained by Ichimaru & Yakimenko (1973); Fuchs et al. (1985) and Rozmus et al. (1987). The continuous interactions of particles with wave packets can be modeled within the quasilinear theory using the Fokker-Planck diffusion equation (Fuchs et al. 1985; Rozmus et al. 1987) given by

$$\frac{\partial f}{\partial t} = \frac{\partial}{\partial \nu} \left( D(\nu) \frac{\partial f}{\partial \nu} \right),\tag{62}$$

where D(v) and f(t, v) are the diffusion coefficient and velocity distribution function respectively and the diffusion coefficient (Fuchs et al. 1985; Rozmus et al. 1987) is given as

$$D(v) = \frac{1}{4} \left(\frac{\varrho}{m_i}\right)^2 l_A \int dk |\delta E_k|^2 \delta(\omega - kv)$$
$$= \frac{1}{4} \left(\frac{\varrho}{m_i}\right)^2 l_A \frac{1}{|v|} |\delta E_k|_{k=\omega/v}^2. \tag{63}$$

Here, Q is the ionic charge and  $l_A$  is the periodicity length. From Equation (31) we can find out the parallel component of the perturbed electric field in Fourier space as

$$\delta E_{zk} = \left[ \frac{\lambda_e^2 \omega k_{0x}}{c} - \frac{v_{te}^2 \lambda_e^2 k_{0x} k_{0z}^2}{c \omega} \right] \delta B_{yk}. \tag{64}$$

The value of  $|\delta E_{zk}|$  for continuously changing k ( $k_{\min} \le k \le k_{\max}$ ), where  $k_{\max}$  and  $k_{\min}$  denote the wavenumbers at the boundaries of the fluctuating field region, can be determined by examining the overall shape of the Fourier spectrum of the magnetic field by using the approximation  $|\delta E_{zk}| = |\delta E_{zk_{\min}}|[|k_{\min}/k|]^{\eta/2}$ . Here,  $\eta$  represents the spectral index of the power spectrum.

In normalized form, Equation (62) can be written as

$$\frac{\partial f}{\partial \tau} = \frac{\partial}{\partial u} \left( D(u) \frac{\partial f}{\partial u} \right),\tag{65}$$

where the velocity is normalized by the thermal velocity of ions,  $v_{\text{thi}} = \sqrt{k_{\text{B}}T_i/m_i}$ , D(v) by  $D(v_0)$ , and f(t, v) by f(0, 0). We used the scale time  $\tau = (v_{\text{thi}})^2/D(v_0)$ , where  $D(v_0)$  is given by

$$D(v_0) = \frac{1}{4} \left(\frac{Q}{m_i}\right)^2 l_A \frac{|\delta E_{k_{\min}}|^2}{v_{k_{\min}}}.$$
 (66)

How the particle distribution function evolves in the presence of stochastic heating has remained unanswered (Chandran et al. 2010; Hoppock et al. 2018). However, we can neglect the time dependence of the distribution function when it reaches a constant value if the observation time  $(t_{obs})$  is much greater than the characteristic time  $(t_d)$  taken to generate the ponderomotive nonlinearity to set up which is of the order of  $r_0/c_s$ , where  $r_0$  is the transverse scale size of the filament of KAWs and  $c_s$  is the ion sound speed. Under this assumption, the particle distribution function is of the form of  $f(v) \propto v^{2+\eta}$ (Sharma & Kumar 2010) where  $\eta$  has a negative spectral slope. In our case  $\eta \approx -3$  and -4 in the dissipation range of the Earth's radiation belt and near-Sun streamer belt solar wind regions, which gives  $f(v) \propto v^{-1}$  and  $f(v) \propto v^{-2}$  respectively. The distribution function is sensitive to the spectral index that leads to the formation of a thermal tail of the energetic particles in the astrophysical plasma.

To solve Equation (65) numerically, we used a Maxwellian distribution function as the initial condition and plotted the distribution function with velocity at different scaled times  $\tau$  ( $\tau$ =0 and  $\tau$ =30) and spectral indices (-5/3 and -3) as displayed in Figure 7. We have chosen  $\tau$ =30 in such a way that, at this scaled time  $t_{\rm obs} \gg t_d$ , the wave spectrum reaches a quasi-stationary state. From Figure 7, it is observed that the fluctuating fields accelerate the particles, hence populating the superthermal tail. The extension of the superthermal tail is dependent on the fluctuating fields and the spectral indices.

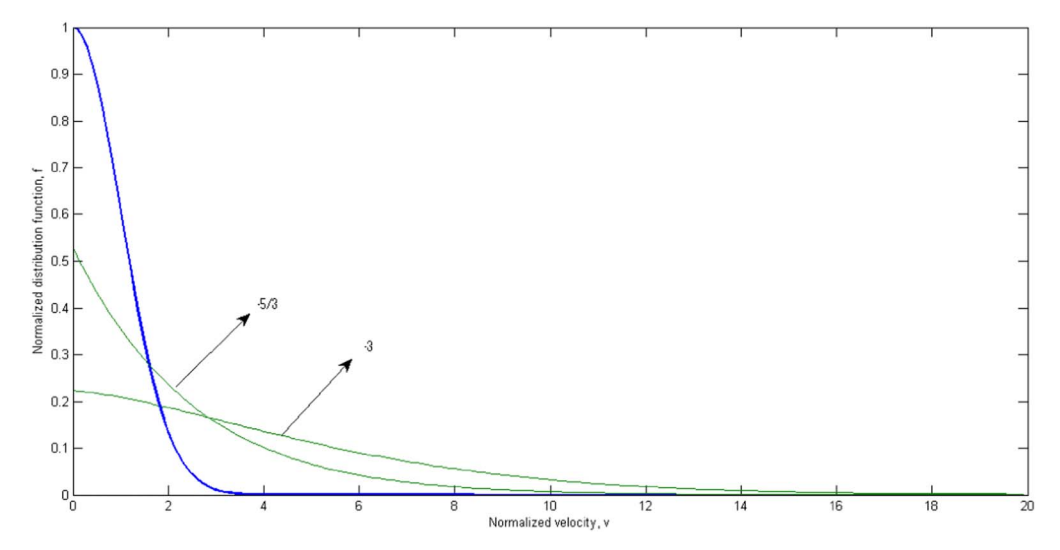


Figure 7. Normalized particle distribution function at scaled times  $\tau = 0$  (blue) and  $\tau = 30$  for spectral indices -5/3 and -3 showing the development of a superthermal tail due to stochastic heating by fluctuating fields.

#### 5. Conclusion

We have numerically analyzed the modified ZSEs governing the coupled dynamics of KAWs and ion acoustic waves applicable to low  $\beta$  < 1, the Earth's radiation belt plasma and high  $\beta > 1$ , near-Sun streamer belt solar wind plasma. The simulations demonstrated the generations of magnetic field filaments or coherent structures due to the density variations produced by the ponderomotive force exerted by the pump KAWs. These magnetic filaments exhibit an initial periodic pattern that evolves into quasi-periodic and chaotic structures over time. The analysis of the magnetic field power spectra reveals a Kolmogorov-like inertial range with a spectral index of -5/3 for scales larger than the ion inertial length, followed by a steeper dissipation range with spectral indices of approximately -3 for the radiation belt plasma and -4 for the near-Sun streamer belt solar wind plasma. In the case of near-Sun streamer belt solar wind, there is an increase in total magnetic power fluctuations and spectral break wavenumber  $k_{\perp}\rho_i \approx 1$ , in comparison to spectral break wavenumber  $k_{\perp}\rho_i \approx 0.76$  in the radiation belt region. The steepening of the spectrum in the dissipation range indicates the transfer of energy from larger to smaller scales, potentially leading to particle energization and heating. Using the quasilinear theory represented by the Fokker-Planck equation and correlating it with the magnetic fluctuation power spectra, we obtained the particle distribution function. We found the extension of the superthermal tail indicating the particle energization that depends on the fluctuating fields and the spectral indices. We studied the following two phenomena independently: (i) generation of turbulence and (ii) heating produced by the wave-particle interaction due to turbulence. However, it has to be studied self consistently by accounting for the energy gained

by the particles in terms of damping of the pump KAW energy. It can be achieved by including a Landau damping term to the pump KAW dynamics as the viscous term is included in the hydrodynamic fluid equation. Moreover, for plasma  $\beta > 1$ , the kinetic effects of Landau damping play a vital role in the waveparticle interaction. Although Landau damping is a purely kinetic phenomenon, there is a way to consider it within the fluid theory as suggested for the first time by Dangelo et al. (1979) to describe its effects on the fast solar wind streams. According to this model, a dissipative term of the form  $\mu \nabla^2 v$ , where  $\mu$  is the damping coefficient, has to be included in the momentum equation. The damping coefficient can be chosen in such a way that it matches the experimentally verified features of kinetic Landau damping. This is the limitation of the present work which we are planning to incorporate in our future work.

### Acknowledgments

The authors are thankful to Sikkim University for providing the centralized High Performance Computational facility at the Brahmagupta Lab. Authors M.K.C. and V.S. are grateful to the University Grants Commission, India for providing a Non-NET fellowship.

## **Data Availability**

The Fortran code to solve the modified ZSEs Equations (52) and (53) is available in Github: https://github.com/hemam12/Pseudo-Spectral-Method and preserved in a repository in Zenodo along with the output data files generated after compiling the code and the MATLAB script files used to plot the figures: 10.5281/zenodo.11096895.

### **ORCID** iDs

Mani K Chettri https://orcid.org/0009-0000-1368-9263 Rupak Mukherjee https://orcid.org/0000-0003-3955-7116

#### References

```
Alazraki, G., & Couturier, P. 1971, A&A, 13, 380
Alexandrova, O., Carbone, V., Veltri, P., & Sorriso-Valvo, L. 2008, ApJ,
Alexandrova, O., Chen, C. H. K., Sorriso-Valvo, L., Horbury, T. S., &
   Bale, S. D. 2013, SSRv, 178, 101
Alexandrova, O., Saur, J., Lacombe, C., et al. 2009, PhRvL, 103, 165003
Aschwanden, M. J., & Parnell, C. E. 2002, ApJ, 572, 1048
Bale, S. D., Balikhin, M. A., Horbury, T. S., et al. 2005, SSRv, 118, 161
Barik, K. C., Singh, S. V., & Lakhina, G. S. 2021, ApJ, 919, 71
Bian, N., Kontar, E., & Brown, J. 2010, A&A, 519, A114
Boldyrev, S., Horaites, K., Xia, Q., & Perez, J. C. 2013, ApJ, 777, 41
Borovsky, J. E. 2012, JGRA, 117, 16
Bowen, T. A., Mallet, A., Bale, S. D., et al. 2020, PhRvL, 125, 025102
Bruno, R., & Carbone, V. 2013, LRSP, 10, 2
Bruno, R., & Trenchi, L. 2014, ApJ, 787, L24
Burlaga, L. F., Scudder, J. D., Klein, L. W., & Isenberg, P. A. 1990, JGRA,
   95, 2229
Canuto, C., Hussaini, M. Y., Quarteroni, A., & Zang, T. A. 2007, Spectral
   Methods: Evolution to Complex Geometries and Applications to Fluid
   Dynamics (Berlin: Springer)
Cattell, C., Wygant, J., Goetz, K., et al. 2008, GeoRL, 35, 13
Chae, J., Cho, K., Nakariakov, V. M., Cho, K.-S., & Kwon, R.-Y. 2021, ApJ,
   914, L16
Chandran, B. D., Li, B., Rogers, B. N., Quataert, E., & Germaschewski, K.
   2010, ApJ, 720, 503
Chaston, C., Bonnell, J., Carlson, C., et al. 2004, JGRA, 109, 19
Chaston, C., Bonnell, J., Clausen, L., & Angelopoulos, V. 2012, JGRA, 117, 2
Chaston, C., Bonnell, J., Halford, A., et al. 2018, GeoRL, 45, 9344
Chaston, C., Bonnell, J., Wygant, J., et al. 2015, GeoRL, 42, 10
Chaston, C. C., Carlson, C. W., Ergun, R. E., & McFadden, J. P. 2000, PhST,
Chaston, C. C., Johnson, J. R., Wilber, M., et al. 2009, PhRvL, 102, 015001
Chaston, C. C., Phan, T. D., Bonnell, J. W., et al. 2005a, PhRvL, 95, 065002
Chaston, C., Peticolas, L., Carlson, C., et al. 2005b, JGRA, 110, 2
Chen, C. H., & Boldyrev, S. 2017, ApJ, 842, 122
Chen, C. H. K., Bale, S. D., Bonnell, J. W., et al. 2020, ApJS, 246, 53
Chen, C., Chandran, B., Woodham, L., et al. 2021a, A&A, 650, L3
Chen, L., Wu, D. J., & Hua, Y. P. 2011, PhRvE, 84, 046406
Chen, L., Wu, D. J., & Huang, J. 2013, JGRA, 118, 2951
Chen, L., & Zonca, F. 2016, RvMP, 88, 015008
Chen, L., Zonca, F., & Lin, Y. 2021b, RvMPP, 5, 1
Cheng, Z. W., Zhang, J. C., Shi, J. K., et al. 2016, JGRA, 121, 3058
Cramer, N. F. 2011, The Physics of Alfvén Waves (New York: Wiley)
Cuseri, I., Mullan, D., Noci, G., & Poletto, G. 1999, ApJ, 514, 989
Dai, L. 2009, PhRvL, 102, 245003
Dangelo, N., Joyce, G., & Pesses, M. E. 1979, ApJ, 229, 1138
Davidson, R. 2012, Methods in Nonlinear Plasma Theory (Amsterdam:
   Elsevier)
Del Zanna, L., & Velli, M. 2002, AdSpR, 30, 471
Dewan, H., Singh, I., Uma, R., & Sharma, R. 2022, PPCF, 64, 095004
Domingo, V. 2002, Ap&SS, 282, 171
Doolen, G., DuBois, D., & Rose, H. A. 1985, PhRvL, 54, 804
Duan, S., Dai, L., Wang, C., et al. 2016, JGRA, 121, 4316
Duan, S., Liu, Z., & Angelopoulos, V. 2012, ChSBu, 57, 1429
Dwivedi, N. K., Batra, K., & Sharma, R. 2012, JGRA, 117, 19
D'Amicis, R., Bruno, R., Panasenco, O., et al. 2021b, A&A, 656, A21
D'Amicis, R., Perrone, D., Bruno, R., & Velli, M. 2021a, JGRA, 126, e28996
Escande, D. F., Gondret, V., & Sattin, F. 2019, NatSR, 9, 14274
Fiksel, G., Almagri, A., Chapman, B., et al. 2009, PhRvL, 103, 145002
Fisk, L. A. 2003, JGRA, 108, 1
Fornberg, B., & Whitham, G. B. 1978, RSPTA, 289, 373
Fuchs, V., Cairns, R., Shoucri, M., Hizanidis, K., & Bers, A. 1985, PhFl, 28, 3619
```

```
Gary, S. P., & Nishimura, K. 2004, JGRA, 109, 19
Gekelman, W. 1999, JGR, 104, 14417
Génot, V., Louarn, P., & Mottez, F. 2000, JGR, 105, 27611
Gershman, D. J., F-Viñas, A., Dorelli, J. C., et al. 2017, NatCo, 8, 14719
Goertz, C. K., & Boswell, R. W. 1979, JGR, 84, 7239
Goossens, M., Erdélyi, R., & Ruderman, M. S. 2011, SSRv, 158, 289
Goyal, R., Sharma, R., & Gupta, D. 2018, PhPl, 25, 13
Grant, S. D., Jess, D. B., Zaqarashvili, T. V., et al. 2018, NatPh, 14, 480
Hasegawa, A. 1976, JGR, 81, 5083
Hasegawa, A., & Mima, K. 1976, PhRvL, 37, 690
Hasegawa, A., & Uberoi, C. 1978, Alfven Wave (New York: Columbia Univ.)
Hashim, P., Hong, Z.-X., Ji, H.-S., et al. 2021, RAA, 21, 105
Heyvaerts, J., & Priest, E. R. 1983, A&A, 117, 220
Hollweg, J. V. 1999, JGR, 104, 14811
Hoppock, I. W., Chandran, B. D., Klein, K. G., Mallet, A., & Verscharen, D.
   2018, JPlPh, 84, 905840615
Howes, G. G., Cowley, S. C., Dorland, W., et al. 2006, ApJ, 651, 590
Huang, S., Sahraoui, F., Andrés, N., et al. 2021, ApJ, 909, L7
Hudson, H. 1991, SoPh, 133, 357
Ichimaru, S., & Yakimenko, I. 1973, PhyS, 7, 198
Johns Hopkins University Applied Physics Laboratory 2023, Parker Solar
   Probe-The Mission
Johnson, J. R., & Cheng, C. 2001, GeoRL, 28, 4421
Johnson, J. R., Cheng, C., & Song, P. 2001, GeoRL, 28, 227
Johnson, J. R., & Cheng, C. Z. 1997, GeoRL, 24, 1423
Kasper, J., Klein, K., Lichko, E., et al. 2021, PhRvL, 127, 255101
Kaur, N., & Saini, N. S. 2016, Ap&SS, 361, 331
Keiling, A., Parks, G., Wygant, J., et al. 2005, JGRA, 110, 2
Kopriva, D. A. 2009, Implementing Spectral Methods for Partial Differential
   Equations: Algorithms for Scientists and Engineers (Dordrecht: Springer)
Kumar, S., Sharma, R., & Singh, H. 2009, PhPl, 16, 3
Larosa, A. 2021, PhD Thesis, Université d'Orléans
Leamon, R. J., Smith, C. W., Ness, N. F., Matthaeus, W. H., & Wong, H. K.
   1998, JGR, 103, 4775
Liewer, P. C., Vourlidas, A., Stenborg, G., et al. 2023, ApJ, 948, 24
Lion, S., Alexandrova, O., & Zaslavsky, A. 2016, ApJ, 824, 47
Liu, Z.-X., He, J.-S., & Yan, L.-M. 2014, RAA, 14, 299
Liu, Z.-Y., Zong, Q.-G., Rankin, R., et al. 2023, NatCo, 14, 2088
López, R. A., Viñas, A. F., Araneda, J. A., & Yoon, P. H. 2017, ApJ, 845, 60
Lotz, S., Nel, A., Wicks, R., et al. 2023, ApJ, 942, 93
Lysak, R., Hudson, M., & Temerin, M. 1980, JGR, 85, 678
Malara, F., Nigro, G., Valentini, F., & Sorriso-Valvo, L. 2019, ApJ, 871, 66
Malaspina, D. M., Chasapis, A., Tatum, P., et al. 2022, ApJ, 936, 128
Markovskii, S., Vasquez, B. J., Smith, C. W., & Hollweg, J. V. 2006, ApJ,
   639, 1177
Matteini, L., Alexandrova, O., Chen, C., & Lacombe, C. 2017, MNRAS,
   466, 945
Matteini, L., Franci, L., Alexandrova, O., et al. 2020, FrASS, 7, 563075
Matthaeus, W. H., Zank, G. P., Oughton, S., Mullan, D. J., & Dmitruk, P.
   1999, ApJ, 523, L93
McComas, D. J., Velli, M., Lewis, W. S., et al. 2007, RvGeo, 45, 2
Moya, P. S., Pinto, V. A., Viñas, A. F., et al. 2015, JGRA, 120, 5504
Nättilä, J., & Beloborodov, A. M. 2022, PhRvL, 128, 075101
Passot, T., Henri, P., Laveder, D., & Sulem, P.-L. 2014, EPJD, 68, 1
Patterson, G., Jr, & Orszag, S. A. 1971, PhFl, 14, 2538
Phillips, K. J. 2000, PPCF, 42, 113
Podesta, J. 2011, JGRA, 116, 16
Popel, S., Vladimirov, S., & Shukla, P. 1995, PhPl, 2, 716
Raghav, A. N., & Kule, A. 2018, MNRAS, 480, L6
Rai, R. K., Sharma, S., Yadav, N., & Sharma, R. P. 2017, PhPl, 24, 2
Ripoll, J.-F., Claudepierre, S., Ukhorskiy, A., et al. 2020, JGRA, 125,
   e2019JA026735
Roberts, D. A. 1990, JGR, 95, 1087
Roberts, O., Narita, Y., Nakamura, R., Vörös, Z., & Verscharen, D. 2022, PhPl,
Roberts, O. W., Narita, Y., Nakamura, R., Vörös, Z., & Gershman, D. 2019,
   FrP, 7, 184
Rozmus, W., Sharma, R., Samson, J., & Tighe, W. 1987, PhFl, 30, 2181
Sadiq, N., Ahmad, M., Farooq, M., & Jan, Q. 2018, PhPl, 25, 4
Šafránková, J., Němeček, Z., Němec, F., et al. 2023, ApJ, 946, L44
```

```
Sahraoui, F., Belmont, G., Goldstein, M. L., & Rezeau, L. 2010, JGRA, 115, 3
Sahraoui, F., Goldstein, M., Robert, P., & Khotyaintsev, Y. V. 2009, PhRvL,
   102, 231102
Saleem, H., & Mahmood, S. 2003, PhPl, 10, 2612
Salem, C. S., Howes, G. G., Sundkvist, D., et al. 2012, ApJ, 745, L9
Schekochihin, A. A., Cowley, S. C., Dorland, W., et al. 2009, ApJS, 182, 310
Shaikh, D., & Zank, G. 2009, MNRAS, 400, 1881
Sharma Pyakurel, P., Shay, M. A., Haggerty, C. C., et al. 2018, JGRA,
   123, 341
Sharma, R., & Kumar, S. 2010, PhLA, 374, 3491
Sharma, R., Stubbe, P., & Verga, A. 1996, JGR, 101, 10995
Shen, Y., & Knudsen, D. J. 2020, JGRA, 125, e2019JA027291
Shi, C., Zhao, J., Huang, J., et al. 2021, ApJ, 908, L19
Shukla, N., Varma, P., & Tiwari, M. S. 2009, IJPAP, 47(05), 355
Shukla, P., & Stenflo, L. 2000a, PhPl, 7, 2738
Shukla, P., Stenflo, L., & Bingham, R. 1999, PhPl, 6, 1677
Shukla, P. K., & Stenflo, L. 2005, PhPl, 12, 8
Shukla, P. K., & Stenflo, L. 2000, in Nonlinear MHD Waves and Turbulence:
   Proc. of the Workshop Held in Nice, France, 1-4 December 1998 (Berlin:
   Springer), 30
Shukla, P. K., Stenflo, L., Bingham, R., & Eliasson, B. 2004, PPCF, 46, B349
Simnett, G. 2005, JGRA, 110, 18
Singh, H. D., & Jatav, B. S. 2019a, RAA, 19, 185
Singh, H. D., & Jatav, B. S. 2019b, RAA, 19, 093
Singh, H., & Sharma, R. 2006, PhPl, 13, 3
Singh, I., Uma, R., & Sharma, R. 2022, Optik, 267, 169698
Singh, M., Singh, K., & Saini, N. S. 2021, Prama, 95, 1
```

```
Sinhababu, A., & Ayyalasomayajula, S. 2021, MatCom, 182, 116
Smith, C. W., Hamilton, K., Vasquez, B. J., & Leamon, R. J. 2006, ApJ,
Song, P., & Vasyliūnas, V. M. 2011, JGRA, 116, 1
Stasiewicz, K., Bellan, P., Chaston, C., et al. 1971, SSRv, 92, 423
Stéfant, R. J. 1970, PhFl, 13, 440
Suzuki, T. K., & Inutsuka, S.-i. 1971, JGRA, 111, 1
Telloni, D., Sorriso-Valvo, L., Woodham, L. D., et al. 2021, ApJ, 912, L21
Terres, M., & Li, G. 2022, ApJ, 924, 53
Tsiklauri, D. 2006, NJPh, 8, 79
Tsiklauri, D. 2012, PhPl, 19, 14
Tu, C.-Y., & Marsch, E. 1995, SSRv, 73, 1
Tu, C.-Y., & Marsch, E. 2001, JGR, 106, 8233
Velli, M. 2003, PPCF, 45, A205
Velli, M., Pucci, F., Rappazzo, F., & Tenerani, A. 2015, RSPTA, 373,
  20140262
Wu, D., Feng, H., Li, B., & He, J. 2016, JGRA, 121, 7349
Xu, S., Huang, S., Sahraoui, F., et al. 2023, GeoRL, 50, e2023GL105463
Yadav, N., & Sharma, R. 2014, SoPh, 289, 1803
Yin, Z., Yuan, L., & Tang, T. 2005, JCoPh, 210, 325
Yinhua, C., Wei, L., & Yu, M. 2000, PhRvE, 61, 809
Zhang, L., Wang, C., Dai, L., Ren, Y., & Lui, A. 2022, JGRA, 127,
  e2021JA029593
Zhao, L.-L., Zank, G., Adhikari, L., et al. 2022a, ApJ, 934, L36
Zhao, L.-L., Zank, G., Telloni, D., et al. 2022b, ApJ, 928, L15
Zhdankin, V., Boldyrev, S., Perez, J. C., & Tobias, S. M. 2014, ApJ, 795, 127
```